The Role of Narrow Cold Frontal Rainbands on Flooding in Urban Southern California

Justin Tang[1*] and Hilary McMillan[1]

[1]*Department of Geography, San Diego State University, San Diego, CA, USA*

[*] jrtang@proton.me

Word Count: 6,091

Peer Review Status:
This is a preprint posted to EarthArXiv. It was previously submitted to *Taylor & Francis Hydrological Sciences Journal* and received a decision of "reject with resubmission possible" after peer review (January 2026). The authors are considering revision options.

Abstract

Narrow cold frontal rainbands (NCFRs) bring brief but intense periods of rain during wintertime extratropical cyclones in Southern California. Much is known about the meteorology behind NCFRs, but little is known about NCFRs that ties together the meteorology and hydrology of urbanized watersheds. In this study, we assessed the extent of flooding in urban Southern California caused by NCFRs. We first quantified the proportion of flood events caused by NCFRs between 1995 to 2020 by analyzing NEXRAD reflectivity data, flash flood warnings (FFWs) issued by the National Weather Service, and USGS streamflow data of NCFR events. Seeking to understand the hydrometeorological characteristics of NCFRs, we then performed a regression analysis and mapped the quantitative precipitation estimation (QPE) data. Our results show that NCFRs make up nearly 40 percent of urban flood events, and that there were significant geographical differences in hydrometeorological characteristics among the four watersheds that warrant further study.

Keywords: narrow cold frontal rainbands; flooding; radar; regression analysis; quantitative precipitation estimation; streamflow; watershed; urban; Southern California

1 Introduction

1.1 Urbanization Impacts on Flooding

Over half of the world's population lives in urban areas, and this proportion is projected to increase to over two-thirds in 2050 (Richie et al., 2024). Urbanization, and associated increases of impervious land cover, increases runoff under heavy rainfall events where the rainfall rate exceeds the capacity of the ground to absorb water and the capacity of storm drains to capture and divert water (Ferguson and Suckling, 1990; Moscrip and Montgomery, 1997; Houston et al., 2011). Globally, flooding is a major cause of death and damage; between 2000 and 2019, flooding accounted for 44% of weather-related disasters, affected 1.65 billion people, killed 104,614 people, and costed $651 billion in economic losses worldwide (UNDRR, 2020). Flooding affects poorer communities and poorer countries disproportionately, whose inhabitants are already at increased vulnerability and sensitivity to such disasters (Braun and Aßheuer, 2011; Fahy et al., 2019; Huong and Pathirana, 2013).

1.2 Meteorological Mechanisms of Narrow Cold Frontal Rainbands

One particular weather phenomenon that can contribute to urban flooding is called the "narrow cold frontal rainband (NCFR)." NCFRs bring the most intense rainfall in an extratropical cyclone and cause flash flooding in the midlatitudes, yet little attention has been paid to their relationship to urban flooding (Houze et al., 1976; Cannon et al., 2020). NCFRs are found in the warm sector of an extratropical cyclone and in front of an approaching cold front. They span 3-5 km in width and extend up to 100-200 km in length. Within these NCFRs, precipitation is divided into "gaps" and "cores." Gaps, which have lengths of between 20 and 50 km, bring lighter precipitation. Cores, which have lengths of 3 to 100 km, bring the most intense precipitation (25+ mm/hr) in an extratropical cyclone. Low-level, nearly perpendicular flow of moisture feed into the cores, and a variety of synoptic and mesoscale mechanisms such as barrier jet, orography, and cloud physics play a role in the development of the NCFR (Hobbs and Biswas, 1979; Collins et al., 2020).

Several meteorological factors can enhance the rain rates of an NCFR. When the transport of atmospheric water vapor is nearly orthogonal to a mountain range, orographic uplifting and heavier precipitation will result (Cannon et al., 2018; Viale et al., 2013). In addition, a “seeder-feeder” mechanism can occur when NCFR updrafts overrun an orographically-induced stratiform cloud, where much lighter precipitation is occurring, causing the “seeder” updraft to drop water or ice droplets through the “feeder” stratiform cloud. As the “seeder” droplets encounter the “feeder” droplets, they combine via accretion or coalescence—causing the droplets to increase in size. These enlarged droplets, as a result, will enhance the NCFR rain rates (Viale et al., 2013).

1.3 Significance of NCFRs in California

NCFRs are responsible for many hydrological and geomorphological hazards in California. One NCFR event led to landslides in the Sierra Nevada foothills on 22 March 2018 as well as significant regional flash flooding, infrastructure damage, and 1-day sediment flux 16 times the average (Collins et al., 2020). On 17 February 2017, an NCFR passing through Southern California contributed to high streamflow at the Santa Ana River and high volumes of water for storage at the Prado Dam. With high amounts of water in both the river and the dam, rapid releases of water were necessary to prevent the dam from exceeding capacity (Cannon et al., 2018). Another NCFR dropped >13 mm of rain in five minutes over Thomas Fire burn scar in Southern California, triggering devastating debris flows over Montecito and Carpinteria that killed 23 people, destroyed 246 structures, damaged 167 structures, and resulted in an estimated residential and commercial property loss of at least $421 million USD (Oakley et al., 2018).

Southern California has a Mediterranean climate characterized by short, wet winters and long, dry summers. Annual precipitation is highly variable, relegated to a few large storms that could make a difference between a wet or dry year (Dettinger et al., 2011). During November through March, rain events typically come as landfalling extratropical cyclones and cold fronts—bringing relatively narrow bands of precipitation. Cold fronts can occasionally induce NCFRs, which are driven and enhanced by Southern California's complex topography via orographic uplifting or low-level coastal convergence (National Research Center, 2005, pp. 15-19). In addition, urban sprawl and development on alluvial fans situated below steep mountains makes the region particularly prone to flash flooding; and it can only take as little as 10 minutes of heavy rain to cause flooding in streams (National Research Center, 2005, p. 83; Oakley et al., 2017; Cannon et al., 2020). Southern California's intense wildfires can render soils hydrophobic in post-fire burn scars, triggering damaging and deadly post-fire debris flows during intense rain events as evident in Montecito and Carpinteria on 9 January 2018 (Oakley et al., 2017; Oakley et al., 2018; Cannon et al., 2020; de Orla Barile et al., 2020).

1.4 Climate Change Projections

Future climate projections indicate an increase in extreme precipitation events (5 to 200 year return interval) and a decrease in non-extreme precipitation events globally (DeAngelis et al., 2015; Manabe and Wetherald, 1975). Higher atmospheric water vapor will cause tropical extremes and large atmospheric river events to increase, allowing storms to deliver heavier precipitation (Thackeray et al., 2018). Along with population growth, increases in extreme precipitation events will lead to greater population exposure to extreme flood potential (Swain et al., 2020).

In Southern California, future projections indicate increased winter precipitation, decreased "shoulder" season (late autumn, early spring) precipitation, and an increased frequency of both extremely wet and dry years leading to greater precipitation "whiplash" (Swain et al., 2018; Huang et al., 2020). A shorter but amplified rainy season will promote greater vegetation growth (and more fuels for fire) in the spring and lead to a longer and increasingly severe fire season (Swain, 2021). With greater vegetation lost to fires, soils and landscapes will become more susceptible to severe runoff response and post-fire debris flows under intense precipitation events (Oakley et al., 2017). While currently no study on the frequency and intensity of NCFRs with respect to climate change appears to exist, there are strong indications that hourly precipitation extremes will intensify and flash flood occurrence will increase globally and in Southern California (Westra et al., 2014; Modrick et al., 2015; Prein et al, 2016).

1.5 Objective of Study

Currently, studies on NCFRs have focused on the atmospheric physics and meteorology, and few studies exist assessing the impacts of NCFRs on hydrological and geomorphological responses. Collins et al. (2020) presents the first such study by linking the mesoscale meteorology of NCFRs with the extreme landscape response of the Sierra Nevada foothills. However, studies linking the meteorology and flood hydrology remain nonexistent. De Orla-Barile et al. (2022) created the first “NCFR catalog” that lists the landfalling NCFRs from 1995-2020 in Southern California—providing new opportunities for the detailed study of NCFRs in the region.

The objective of this study is to assess the extent to which NCFRs cause flash flooding in urban Southern California. To meet the objective, the study is split into two sections. The first section involves finding the proportion of flash flood events in selected urban watersheds of Southern California that are caused by NCFRs. The second section involves assessing the hydrometeorological characteristics of NCFRs that are linked with urban flooding. These findings will be used to address the knowledge gaps pertaining to the flood hydrology and hydrometeorology of NCFRs in Southern California.

2 Materials and Methods

2.1 Study area

In this paper, urban Southern California refers to both the Los Angeles and the San Diego metropolitan areas. The Los Angeles metropolitan area is comprised of Los Angeles, Orange, southwestern San Bernardino, and western Riverside Counties. Altogether, the metropolitan area covers a total land area of 87,940 km^2 (33,945 mi^2), which is the largest metropolitan area in the United States. (Fig. 1). The topography is varied and complex—consisting of coastal plain, foothills, valleys, mountains, and deserts. The elevation can range from sea level in the coastal plain to 3,068 m (10,064 ft) at the summit of Mount San Antonio (San Gabriel Mountains). Annual mean precipitation is approximately 394 mm (15.5 in) in the coastal plain, 836 mm (32.9 in) in the mountains, 198 mm (7.8 in) in the desert/Antelope Valley (Wolfe et al., 2006).

The San Diego metropolitan area covers a total land area of 10,900 km^2 (4,207 mi^2), including 113 km (70 mi) of coastline. Most urban and residential development are near the coast in the south and west, whereas the eastern half of the county remains relatively undeveloped (Fig. 1). Like the Los Angeles metropolitan area, the surrounding topography consists of coastal plain, foothills, valleys, and mountains, and deserts. The elevation can range from sea level toward the west to 900-1,500 m (3,000-5,000 ft) toward the east. Annual mean precipitation is approximately 254 mm (10 in) near the coast, 762 mm (30 in) in the mountains, and 76.2 mm (3 in) in the eastern valley floor (San Diego Flood Control Advisory Commission, 2003).

For the purposes of this research, the hydrometeorological assessment was focused on the dense impervious areas of the Los Angeles and San Diego metropolitan areas—largely excluding the foothills, mountains, and deserts. However, the surrounding areas and topography were used to aid the analysis as well as classifying NCFR flood events (see section 3)

2.2 Data

2.2.1 NWS Watches, Warnings, and Advisories

We obtained NWS Watches, Warnings, and Advisories (WWAs) from a WWA Catalog from de Orla-Barile et al. (2022). Each entry in the Catalog indicates a flash flood, severe thunderstorm, or tornado warning issued (as “NEW”) by either the Los Angeles/Oxnard (LOX) or San Diego (SGX) Weather Forecast Offices (WFOs) between 1995-2020, which came from the Iowa State University Iowa Environmental Mesonet Archive (https://mesonet.agron.iastate.edu/request/gis/watchwarn.phtml). Flash flood warnings (FFWs), which we analyze in this study, are public warnings that indicate extreme weather conditions that can be associated with NCFRs (de Orla-Barile et al., 2022; Oakley et al., 2018; Sukup et al., 2016; Thompson, 2001). FFWs are issued “when flooding is imminent or likely” (80%+ confidence) within a 24-36 hour period, and the defined geographical area—as denoted by a polygon—may encompass all or a portion of that area (US Department of Commerce, n.d.). Typically, a WFO will issue a FFW when flash flooding is already reported, precipitation capable of flash flooding is indicated on radar, and/or flash flooding in a small stream is indicated by a hydrologic model.

2.2.2 Streamflow measurements

Streamflow measurements from each WFO were obtained from the USGS National Water Information System (NWIS). Four sites were used, two for each WFO, and are listed as follows: Sepulveda Dam, Van Nuys (Gauge #: 11092450; WFO: LOX); Whittier Narrows Dam, Pico Riviera (Gauge #: 11101250; LOX); Santa Ana R A (Gauge #: 11078000; WFO: SGX); and San Diego R A Fashion Valley (Gauge #: 11023000; WFO: SGX) (Fig. 1). These USGS NWIS sites are located downstream of highly urbanized watersheds and can serve as an indicator for urban flooding (Table 1).

2.2.3 Rainfall measurements

We used observed rainfall totals from the Remote Automated Weather Station (RAWS) climate archive during the period of 1995-2020. The RAWS climate archive contains in the United States 1,850 stations that collect hourly weather data and transmit them via satellite back to the National Interagency Fire Center (NIFC). We used four RAWS sites, one representing each watershed, that were selected based on their proximity to urban development and to the center of the watershed as well as data availability during the 1995-2020 time period (Table 5). Note that the Sepulveda Dam USGS gauge and the Camp Elliot (San Diego watershed) RAWS site only had available data starting from 2002 and 2004, respectively, which meant that streamflow and rainfall data were limited for those two watersheds. For NCFRs that impacted the region overnight—that is, the NCFR start and end time fell on two different days—we used the mean of the daily discharge and precipitation over a two-day period.

Gridded Quantitative Precipitation Estimation (QPE) data were obtained from the Oak Ridge National Laboratory Distributed Active Archive Center (ORNL DAAC) for Biogeochemical Dynamics, which is a NASA Earth Observing System Data and Information System (EOSDIS) data center. The ORNL DAAC contains Daymet Version 4 data as gridded estimates of daily weather parameters at a 1 x 1 km spatial resolution in North America, Hawaii, and Puerto Rico (Thornton et al., 2020). These gridded estimates were derived from interpolating and extrapolating ground-based observations from statistical modeling techniques.

2.2.3 NCFR Catalog

We used the NCFR catalog created by de Orla-Barile et al. (2022) that contains a list of NCFR events that made landfall in Southern California between 1995 and 2020 (events in 2020 ran from January to May only). Items in the NCFR catalog included propagation statistics, Next Generation

Weather Radar (NEXRAD) composite plots, and ERA5 (European Center for Medium-Range Weather Forecasting, 5th generation) reanalysis plots (see Table 3 for explanation of these items). De Orla-Barile et al. (2022) identified 76 NCFRs during this time period that led to the issuance of 279 flash flood warnings. Processed reflectivity data of NCFR events at 5-minute intervals also came from de Orla-Barile et al. (2022). De Orla-Barile et al. (2022) originally obtained the data from the Amazon Webs Services Archive, which contains NEXRAD level-II data since 1991 (*https://registry.opendata.aws/noaa-nexrad/*) and then processed and gridded the data using the Lidar Radar Open Software Environment (LROSE; *http://lrose.net/software.html*). NCFRs were identified using criteria as specified in de Orla Barile et al. (2022), Jorgensen et al. (2003), Hobbs and Biswas (1979), and Houze et al. (1976). That is, areas of high reflectivity (>=45 dbz), narrow (several kilometers) but elongated (tens to thousands of kilometers) cells, and a “gap and core” structure were sought after in radar imagery. In total, there were 78 NCFRs and associated datasets between 1995 and 2020.

2.3 Methods

2.3.1 Identifying urban flash flood events

Finding the proportion of flash flood events in urban Southern California that are caused by NCFRs requires identification of the flash flood events and what constitutes a flash flood event specific to urban Southern California. First, using the NWS WWA archive, we identified days where either of the WFOs issued a flash flood warning. We selected only warnings that occurred during the months of October to June. We excluded warnings from July to September because NCFRs do not typically occur during these months and because flash flood warnings issued during the summer are mostly due to monsoonal thunderstorms (Houze et al., 1976; Hobbs and Biswas, 1979; Viale et al., 2013; Cannon et al., 2020; Collins et al., 2020; de Orla-Barile et al., 2022).

On days when a WFO issued a flash flood warning, we checked whether peak streamflow at the selected USGS gauges was higher than the median (2-year recurrence interval) of the annual peak streamflows (Table 2). To find the median, we used a flood frequency analysis based on the Weibull plotting position method (Fig. 2). Once we established the streamflow threshold, we counted the number of flood events during the 1995-2020 period. To process the 1,798 WWAs and 25 years of 15-minute interval streamflow data, we developed a Python script to automatically identify streamflows that exceed the threshold during a FFW. If either of the WFO (LOX or SGX) issued or extended a FFW and at least one of the urban watersheds corresponding to the WFO reported streamflows exceeding the threshold during the time frame, then the event was classified as a flood event in urban Southern California. Flood events were counted on a daily basis. That is, two or more instances of flooding on a single day was counted a single event; but events occurring on two (or more) consecutive days were counted as two (or more) flood events.

2.3.2 Identifying NCFRs co-occurring with flash flood events

To identify whether or not an NCFR has caused a flood event in urban Southern California, we first sought to identify the spatial boundaries of each NCFR on the processed reflectivity data from the NCFR Catalog (Table 3) and developed a Python algorithm to facilitate identification (Tang, 2025). We followed the methods of Haberlie and Ashley (2018) who employed a segmentation procedure to delineate the boundaries of a Mesocale Convective System (MCS) on radar imagery and applied it to the delineation of NCFR cores.

Our algorithm follows a seven-step procedure that employs a variety of mathematical morphological techniques—such as image labeling and binary closing—to determine whether the boundaries of an NCFR core intersect with the chosen watershed boundaries (Table 4; Fig. 3). When using the algorithm for all events, NCFRs were detected via a mixed automated and manual procedure. Because the algorithm used fixed thresholds (e.g. it requires that the NCFR should have a “gap and core” structure, have reflectivity >= 45 dbZ, and have a narrow and elongated shape), the algorithm occasionally misidentified cores or failed to identify cores. Therefore, we used a second manual quality control step to ensure accuracy. In this step, we adjusted reflectivity thresholds where necessary to properly identify cores. For example, while established literature reports that cores have at least 45 dbZ reflectivity; in actuality, some storms had NCFR cores with lower reflectivities embedded within them such as at >=35 dbZ or >=40 dbZ.

Once the NCFR cores were delineated on radar imagery, we established a link between the NCFR event and urban flooding through a multi-step process. First, NCFR events with at least one matching FFW were identified (Fig. 4). A FFW is defined as matching when its start time falls within an NCFR start and end time or up to 2 hours and 50 minutes after the NCFR end time. FFWs can be issued up to several hours after heavy rain, including after the end of an NCFR passage; therefore, the 2 hour, 50 minute time period functions as the “lag time” between the NCFR passage and the streamflow response. This number was calculated by finding the mean time length of the FFWs in the WWA Catalog, which should sufficiently cover all FFWs caused by NCFRs—given the short duration of NCFRs (approximately 15 minutes) and their “flashiness” (i.e. ability to cause sharp rises in streamflow).

Second, for the 48 NCFR events with at least one matching FFW, radar imagery was assessed—after using the segmentation procedure described above—to identify events where NCFR cores intersect with one of our study watersheds (Table 8). Intersections were determined using Python package shapely.geometry by polygonizing the NCFR cores and calculating the intersection between the polygonized NCFR cores and the polygon watersheds (Fig. 5) (Tang, 2025).

2.3.3 Identifying NCFR-caused flood events

To identify events where the NCFR caused streamflow to increase past the threshold flow, we required that (1) the flow was below the threshold prior to the time where the NCFR maximally intersects with the watershed (the timestep with the greatest area of intersection on radar imagery), and (2) the flow was above the threshold following the NCFR passage (Fig. 6). Note that the time between the NCFR passage and the peak streamflow is relatively consistent for each watershed; for example, the average streamflow response time for the Santa Ana River watershed is 2 hours and 30 minutes (Table 11). The first criterion helps ensure that the high streamflow is not related to non-NCFR conditions, such as longer duration stratiform rain falling on saturated soils, where earlier meteorological and hydrological conditions likely have played a larger role in flooding than the NCFR itself. NCFR events meeting both criteria (Fig. 7) were considered as the cause of a flood event.

Once list of NCFR flood events were compiled, the number of NCFR flood events was divided by the total number of flood events, calculated in section 2.3.1, during the time period to find the proportion of NCFR flood events in urban Southern California.

2.3.4 Hydrometeorological Characteristics of NCFRs – Linear Regression Analysis

Understanding the hydrometeorological characteristics (i.e. the interrelationships between meteorology and hydrology) is useful for the improvement of short and long-range hydrologic forecasts. Following previous hydrometeorological analyses of storm systems (Smith et al., 2005; Yang et al., 2016; Yang et al., 2016), we used rainfall, radar and streamflow data to analyze the spatial and temporal characteristics of NCFRs and the subsequent storm event response of the urban Los Angeles and San Diego regions. We modeled the relationships between meteorological predictor and hydrological response variables using regression analyses. During the first part of the hydrometeorological analyses, least squares linear regressions were performed and are represented in the form

$$Y = \alpha_0 + \alpha_1 X + \varepsilon \tag{1.1}$$

where α_0 and α_1 are the regression coefficients, X is the predictor variable, ε is the random variable (error term), and Y is the response variable. The regression coefficients α were estimated using matrix multiplication, as represented as

$$\alpha = (X^T X)^{-1} X^T Y \tag{1.2}$$

where α_1 is the regression coefficient, X is the predictor variable and X^T is the transposition of X, and Y is the predictor variable. The R^2 value was obtained via the equation

$$R^2 = 1 - \frac{SSres}{SStot} = 1 - \frac{d(y, Y)}{d(y, \bar{y})} \tag{1.3}$$

where SSres is the residual sum of squares and SStot is the total sum of squares and d(·,·) is the Euclidean distance, y is the actual values of the response dataset, and $\bar{y}$ is the sample mean.

Of the 88 NCFR events with available maximum reflectivity data, we evaluated the relationships between maximum reflectivity and peak discharge, maximum reflectivity and runoff ratio, and total event rainfall and runoff. These relationships help us better understand to what extent the characteristic small-scale, high-intensity rainfall of the NCFR as shown by maximum reflectivity on radar imagery has on the streamflow response and its variability among the urbanized Southern California watersheds. We chose linear and multiple regression models for their simplicity; given their relatively few parameters, they can provide insight into the hydrometeorological relationships over the complex Southern California terrain without the expense of further complications (Beven, p. 66). Maximum reflectivity refers to the maximum value recorded over any of the urban watersheds of interest. We calculated the runoff ratio by dividing the runoff—which was obtained by dividing the daily discharge by the drainage area of the watershed—by the precipitation of the corresponding rain gauge (Table 13).

2.3.5 Hydrometeorological Characteristics of NCFRs – Multiple Regression Analysis

Multiple regression analysis of 30 NCFR events was used to determine the effects of multiple meteorological NCFR characteristics on hydrological response. de Orla Barile et al. (2020) calculated NCFR propagation statistics (distance, storm direction or azimuth, and storm speed) for 10 NCFR events; we followed their method to calculate the same statistics for 20 additional NCFR events to ensure that the sample size was large enough for statistical analysis (Table 14). The method tracks an NCFR core over a 1-hour period, recorded the start and end position of the core's centroid, and calculated the inverse, geodetic distance and azimuth between the two latitude and longitude coordinates. The speed was determined by dividing the distance by the time interval. To obtain the start and end position of the core's centroid, a mixed manual and automatic approach was used. The segmentation procedure was used to automatically track and identify the cores, while manual verification was used to ensure that the core tracked was the same core over time. The 20 selected NCFR events represented all those events where single cores could be tracked over a 1-hour period, sufficient to calculate the propagation statistics.

Multiple linear regressions were performed to assess the relationships between meteorological (predictor) and hydrological (response variables). Predictor variables were maximum reflectivity, azimuth (storm direction), and speed, and response variables were peak streamflow and runoff ratio. A multiple linear regression is represented as

$$\boldsymbol{Y} = \alpha_0 + \alpha_1 \boldsymbol{X}_1 + \alpha_2 \boldsymbol{X}_2 + \ldots\ldots + \alpha_i \boldsymbol{X}_i + \varepsilon \qquad (2.1)$$

Each k^{th} observation would be represented as

$$\boldsymbol{Y}_k = \alpha_0 + \alpha_1 \boldsymbol{X}_{k1} + \alpha_2 \boldsymbol{X}_{k2} + \ldots\ldots + \alpha_i \boldsymbol{X}_{ki} + \varepsilon_k \qquad (2.2)$$

Following the same steps as Section 2.2.4, the regression coefficients and R^2 value can be obtained for multiple variables after performing matrix multiplication. p-values were used to test for statistical significance. Multicollinearity was assessed via the Pearson's correlation coefficient and the variance inflation factor (VIF) to provide insight into the linear relationships between the meteorological variables.

2.3.6 Hydrometeorological Characteristics of NCFRs – QPE Analysis

Using the QPE data, we loaded the precipitation data for every NCFR event in the Catalog, aggregated them to obtain the precipitation for the entire 1995-2020 time period, performed simple arithmetic operations, and plotted the results as maps for the entirety of Southwestern California. The first of the two maps was the percent of normal annual precipitation (NCFRs were grouped by years), which was determined by dividing the aggregated precipitation from NCFR events by the total precipitation based on the climatological mean for the same period. The second map was the average total precipitation per NCFR event, which was determined by dividing the aggregated NCFR precipitation by the number of NCFR events during the same period. We qualitatively assessed the maps to better understand the spatial patterns and distribution of rainfall—especially given the complex topography and microclimates of Southern California—from NCFR events.

3 Results

3.1 Identifying urban flash flood events

Processing 1,798 WWAs in the catalog and 25 years of 15-minute interval streamflow data, we found a total of 221 unique FFWs (not counting entries that indicate a "continued" or expired FFW). Of the FFWs, 28 of them had at least one (of the four) watershed where the streamflow exceeded the flood threshold. Therefore, based on the aforementioned criteria, a total of 28 flood events meriting a FFW and with streamflow above the median annual peak flow occurred in the four watersheds during the 1995-2020 time period.

3.2 Identifying NCFRs co-occurring with flash flood events

We used three iterations of the segmentation algorithm described in Section 2.3.2 to delineate NCFR cores from the radar reflectivity loops in the NCFR Catalog. During the first iteration, approximately 31 storm events had successfully delineated NCFR cores based on the standard thresholds and parameters. Another 31 storm events showed no returns, and 16 storm events showed spotty NCFR core detection. A second iteration—which used modified threshold values (Table 4) that were assessed via trial and error—sought to address the 31 storm events with no returns, and a third iteration sought to improve detection of the 16 storm events. Overall, the algorithm detected defined NCFR core structures propagating through the region for at least several frames in 57 storm events. 11 storm events had segmented NCFRs but still had issues with identification—such as many frames where the algorithm failed to identify the cores or delineated non-NCFR features as NCFR cores—that required manual input. Lastly, the algorithm failed to properly identify the NCFR cores of 11 storm events, necessitating manual identification and verification. The results show that while an automatic segmentation procedure based on fixed thresholds can reasonably identify NCFRs in a majority (~73%) of storm events, there are limitations that require manual identification in a considerable number of storm events (~27%). Because the radar reflectivity loops contain NCFRs previously identified by de Orla-Barile et al. (2022), the distinct and elongated “gap and core” feature was sufficiently visible for manual identification.

Following the segmentation step, we found that 48 of 78 NCFR events had at least one matching FFW, and 57 NCFR events intersected with at least one watershed as outputted by the segmentation procedure (Table 8). 32 NCFR events had at least one matching FFW and an intersection with at least one watershed.

3.3 Identifying NCFR-caused flood events using watershed time of concentration

In total, 12 NCFR events had peak streamflows that exceeded the flood threshold in at least one watershed; and 4, 3, 5, and 5 NCFR events met such criterion in the Sepulveda Dam, Whittier Narrows, Santa Ana River, and San Diego River watersheds respectively (Tables 9-12). 11 NCFR events had peak streamflows above and initial streamflows below the flood threshold in at least one watershed, and 1, 3, 5, and 5 NCFR events met such criteria in the Sepulveda Dam, Whittier Narrows, Santa Ana River, and San Diego River watersheds respectively. As such, these 11 NCFR events were classified as NCFR flood events. For the 1995-2020 time period, dividing the 11 NCFR flood events by the 28 total flood events yields 39% of flood events caused by NCFRs.

3.4 Hydrometeorological Characteristics of NCFRs – Linear Regression Analysis

Figures 8-9 show the linear regression between maximum reflectivity and peak streamflow or runoff ratio of the four watersheds. The R^2 values were all below 0.11, which indicates that less than 11 percent of the variation in peak streamflow or runoff ratio can be attributed to maximum reflectivity. We noted differences in R^2 values between the Northern (Sepulveda Dam and Whittier Narrows Dam) and Southern (Santa Ana and San Diego River) watersheds. Many factors could play a role in these differences—such as differences in the radar tilt and beam blockage, Z-R relationships, discharge measurement method and physical characteristics of the watersheds.. R^2 values were significantly higher for rainfall vs. runoff—with values at 0.53, 0.48, 0.30 and 0.52 for the Sepulveda Dam, Whittier Narrows Dam, Santa Ana River, and San Diego River Watersheds (Figs. 10). Therefore, despite NCFRs being characterized by their high-intensity cores, for all watersheds the rainfall depth that falls during an NCFR event is a much stronger predictor of the subsequent runoff than is the rainfall intensity (as approximated by maximum reflectivity).

3.5 Hydrometeorological Characteristics of NCFRs – Multiple Regression Analysis

Table 6 shows the regression coefficients, p-values, and R^2 values for multiple regressions of maximum reflectivity, azimuth and speed against peak streamflow. Overall, there were significant variations between each watershed; the three predictor variables were the strongest predictors of peak streamflow in the Sepulveda Dam and San Diego River watersheds (0.32 and 0.24 R^2, respectively). However, the three predictor variables were weak predictors ($R^2 < 0.10$) of peak streamflow in the Whittier Narrows Dam and Santa Ana River watersheds (0.10 and 0.07 R^2, respectively). Table 7 shows the multiple linear regressions using the same predictors to predict runoff ratio. The R^2 values were higher overall—at 0.48, 0.26, 0.34 and 0.24 for the Sepulveda Dam, Whittier Narrows Dam, Santa Ana River, and San Diego River watersheds respectively. The p-values for most variables exceeded 0.05—suggesting that the predictor variables do not have a statistically significant relationship with the peak streamflow or runoff ratio. An analysis on multicollinearity via the Pearson's correlation coefficient and the variable inflation factor found that almost all of the variables have low multicollinearity. The one exception is maximum reflectivity, azimuth, and speed vs. runoff ratio in the Sepulveda Dam watershed which had a Pearson correlation coefficient of 0.515 between maximum reflectivity and speed but a variation inflation factor of less than 1.5 for all variables. These results suggest that the NCFR speed and direction have additional predictive value over maximum reflectivity, however not obtaining statistical significance.

3.6 Hydrometeorological Characteristics of NCFRs – QPE Analysis

In the QPE analysis, NCFR events contributed 12-30% of the annual precipitation throughout Southwestern California, with significant geographical variations (Fig. 11). Areas closer to the Transverse Ranges, particularly near the Santa Monica Mountains where the Sepulveda Dam watershed is located, received a higher percentage of their average annual precipitation to NCFR events at 24-30%. The Inland Empire, which encompasses a large portion of the Santa Ana River watershed, received a lower percentage of their annual precipitation to NCFR events at 12-20%. Figure 12 also shows that, on average, NCFRs produce 18-36 mm of rain per event in the Los Angeles metropolitan area and 12-24 mm in the San Diego metropolitan area.

4 Discussion

This study was the first to create and use an automated detection method to identify NCFRs on radar imagery—providing a quicker and more streamlined approach. In addition, this study assessed the relationships between the meteorological characteristics of landfalling NCFR events and the hydrological streamflow response. Both of these results would aid flood forecasting and our general hydrological knowledge of NCFR impacts in urban areas throughout Southern California. Ralph et al. (2014) found that improved flood forecasts of AR events could bring benefits “as much as a third of all residential damages” and “have estimated values that could exceed $100 million in a single year.” NCFRs, which we have shown to significantly increase streamflows and contribute to urban flooding in Southern California, are important for forecast-informed reservoir operations (FIRO)—which could maximize flood control and enhance water storage, offsetting the need for new storage facilities and saving money.

Previous studies on NCFRs have investigated their impacts in Southern California; their meteorological characteristics using observations and models; their climatological characteristics such as frequency and impact (de Orla-Barile et al., 2022); and manual delineation of NCFRs and other convective lines (e.g. MCS) on radar imagery. This paper adds to the literature by proposing automated methods for identifying and tracking NCFRs in Southern California, and clarifying NCFR impacts in Southern California, particularly the hydrologic response in urbanized watersheds. Our results evaluate the climatological characteristics of NCFRs by revealing information of their flood frequency and impacts; and providing a mixed radar and automated based record of NCFRs that gives insights on how to better identify NCFRs on radar imagery.

Hydrometeorological analyses based on radar-based records, however, have their limitations that could have impacted the results. De Orla-Barile et al. (2022) state “the potential for not identifying NCFR events” in automated procedures, which we have approached using mixed automatic-manual methods. Ralph et al. (2014) noted that QPE analyses based on NEXRAD radars are “hamstrung by their siting and scanning strategies, which often miss shallow rain or misinterpret virga aloft as rainfall at the surface, or use inappropriate drop-size distributions.” In addition, they noted that NEXRAD network have better coverage and less beam blockage in the Great Plains than in the mountainous West. Future studies could explore different methods—combining remote sensing, in situ collection and hydrologic modelling methods—to assess hydrometeorological relationships between NCFRs and urbanized watersheds and conduct in depth analyses that better pair meteorological and hydrological streamflow response variables.

5 Conclusion

This study assessed the role of NCFRs on urban flooding in Southern California and the hydrometeorological characteristics of landfalling NCFRs. We developed a new algorithm to delineate NCFR cores on radar imagery, enabling us to identify time periods when NCFR intersect watersheds of interest. To establish whether or not an NCFR caused flooding in Southern California, we checked whether an NWS WFO issued a FFW during the same time frame as the NCFR-watershed intersection and whether the streamflow exceeded the flood threshold (median of the peak annual streamflows) for the watershed. NCFRs meeting such criteria were compared to the total number of flood events—established based on the days when a WFO issued a FFW and the streamflow exceeded the flood threshold—during the 1995-2020 time period to obtain a proportion of flood events caused by NCFRs in urban Southern California. Our results showed that NCFRs made up 39% of the flood events, demonstrating their importance in understanding the causes of urban floods in Southern California.

We studied the hydrometeorological characteristics via linear and multiple linear regressions of meteorological and hydrological variables as well as the mapping of QPE data in the region for the entire time period. Maximum reflectivity (an indicator of rainfall intensity) was not a significant predictor of peak streamflow and runoff ratio in our watersheds, but storm speed and azimuth were predictors of peak streamflow and runoff ratio in some watersheds—where slower-moving storms and storms coming from a slightly more westerly than southerly direction resulted in higher runoff ratios. In the QPE analysis, the contribution of NCFR events to region-wide, average annual precipitation varied significantly; and NCFRs generally produced more rain per event in the Los Angeles metropolitan area than the San Diego metropolitan area.

This study is the first to combine both meteorological and hydrological analyses of NCFRs and to investigate their regional impacts on urban watersheds. Building on past manual approaches, it extended the work of de Orla-Barile et al. (2022) to develop a mixed manual and automated approach to delineating NCFR cores on radar imagery. Through the assessment of NCFR flood impacts in urban Southern California watersheds, regression analyses between meteorological characteristics and hydrological response variables, and QPE analysis of the spatial and geographical distribution of precipitation from NCFR events, this study provided new knowledge on NCFR climatology—which could aid flood forecasting and control in the region.

Acknowledgments

Special thanks are given to Trent Biggs (Department of Geography), Hassan Davani (Department of Civil Engineering), and the Blue Gold Graduate Group at San Diego State University for providing feedback. The authors also thank and acknowledge Forest Cannon, Nina Oakley, and Marian de Orla Barile—who are formerly or currently with the CW3E group at the Scripps Institution of Oceanography—for providing the tools, code, and data to complete the project.

Disclosure statement

No potential conflict of interest was reported by the authors.

Funding

The work was supported by the Department of Geography at San Diego State University.

ORCID

Justin Tang https://orcid.org/0009-0002-2944-9664

Hilary McMillan https://orcid.org/0000-0002-9330-9730

References

Alex. (2017, July 18). Top 50 US Metro Areas By GDP. *Vivid Maps*. https://vividmaps.com/top-50-us-metro-areas-by-gdp/

Bae, S., & Chang, H. (2019). Urbanization and floods in the Seoul Metropolitan area of South Korea: What old maps tell us. *International Journal of Disaster Risk Reduction, 37*, 101186. doi:10.1016/j.ijdrr.2019.101186

Beven, K. J. (2012). *Rainfall-Runoff Modelling: The Primer* (2nd ed.). Wiley-Blackwell.

B. Braun, T. Aßheuer, Floods in megacity environments: vulnerability and coping strategies of slum dwellers in Dhaka/Bangladesh, Nat. Hazards 58 (2011) 771–787. doi.org/10.1007/s11069-011- 9752-5

Blume, T., Zehe, E., & Bronstert, A. (2007). Rainfall—Runoff response, event-based runoff coefficients and hydrograph separation. *Hydrological Sciences Journal*, *52*(5), 843–862. https://doi.org/10.1623/hysj.52.5.843

California Department of Water Resources. (n.d.). *Mapping Tools*. Retrieved January 1, 2022, from https://water.ca.gov/Work-With-Us/Grants-And-Loans/Mapping-Tools

Cannon, F., C. Hecht, J. Cordeira, and F.M. Ralph, 2018: Synoptic to mesoscale forcing of extreme precipitation in Southern California. J. Geophys. Res. Atmos., 123, 13714–13730.

Cannon, F., N. Oakley, A. Michaelis, C. Hecht, B. Kawzenuk, R. Demirdjian, M. Fish, A. Wilson, and F.M. Ralph, 2020: Observations and Predictability of a High-Impact Narrow Cold-Frontal Rainband over Southern California. Weather and Forecasting. 1-40.

Cannon, S. H., Boldt, E. M., Kean, J. W., Laber, J. L., & Staley, D. M. (2010). *Relations Between Rainfall and Postfire Debris-Flow and Flood Magnitudes for Emergency-Response Planning, San Gabriel Mountains, Southern California* (Open-File Report No. 2010–1039; p. 31). U.S. Geological Survey. https://pubs.usgs.gov/of/2010/1039/

Cannon, S. H., Gartner, J. E., Wilson, R. C., Bowers, J. C., & Laber, J. L. (2008). Storm rainfall conditions for floods and debris flows from recently burned areas in southwestern Colorado and southern California. *Geomorphology*, *96*(3), 250–269. https://doi.org/10.1016/j.geomorph.2007.03.019

Collins, B. D., Oakley, N. S., Perkins, J. P., East, A. E., Corbett, S. C., & Hatchett, B. J. (2020). Linking Mesoscale Meteorology With Extreme Landscape Response: Effects of Narrow Cold Frontal

Rainbands (NCFR). *Journal of Geophysical Research: Earth Surface*, *125*(10). doi:10.1029/2020jf005675

Costa, J. E. (1987). Hydraulics and basin morphometry of the largest flash floods in the conterminous United States. *Journal of Hydrology*, *93*(3), 313–338. https://doi.org/10.1016/0022-1694(87)90102-8

DeAngelis, A. M., Qu, X., Zelinka, M. D., & Hall, A. (2015). An observational radiative constraint on hydrologic cycle intensification. *Nature*, *528*(7581), 249-253. doi:10.1038/nature15770

de Orla-Barile, M., Cannon, F., Oakley, N. S., & Ralph, F. M. (2022). A Climatology of Narrow Cold-Frontal Rainbands in Southern California. *Geophysical Research Letters*, *49*(2), e2021GL095362. https://doi.org/10.1029/2021GL095362

Department of Public Works. (n.d.). *Seven Oaks Dam*. San Bernardino County. Retrieved November 3, 2022, from https://dpw.sbcounty.gov/flood-control/seven-oaks-dam/

Dettinger, M. D., Ralph, F. M., Das, T., Neiman, P. J., & Cayan, D. R. (2011). Atmospheric rivers, floods and the water resources of California. *Water, 3*(2), 445-478. doi:10.3390/w3020445

Dingman, S. L. (2015). *Physical Hydrology*. Waveland Press.

Fahy, B., Brenneman, E., Chang, H. and Shandas, V., 2019. Spatial analysis of urban flooding and extreme heat hazard potential in Portland, OR. *International journal of disaster risk reduction*, *39*, p.101117.

Ferguson, B.K. and Suckling, P.W., 1990. Changing rainfall-runoff relationships in the urbanizing Peachtree creek watershed, Atlanta, Georgia. JAWRA Journal of the American Water Resources Association, 26(2), pp.313-322.

Haberlie, A. M., & Ashley, W. S. (2018). A Method for Identifying Midlatitude Mesoscale Convective Systems in Radar Mosaics. Part I: Segmentation and Classification. *Journal of Applied Meteorology and Climatology*, *57*(7), 1575–1598. https://doi.org/10.1175/JAMC-D-17-0293.1

Hobbs, P. V., & Biswas, K. R. (1979). The cellular structure of narrow cold-frontal rainbands. *Quarterly Journal of the Royal Meteorological Society*, *105*(445), 723-727. doi:10.1002/qj.49710544516

Houston, D., Werritty, A., Bassett, D., Geddes, A., Hoolachan, A., & McMillan, M. (2011). *Pluvial (rain-related) flooding in urban areas: The invisible hazard* (pp. 3-95, Rep. No. 978-1-85935-863-4). York, UK: Joseph Rowntree Foundation.

Houze, R. A., Jr., Hobbs, P. V., Biswas, K. R., & Davis, W. M. (1976). Mesoscale Rainbands in Extratopical Cyclones. *Monthly Weather Review, 104*, 868-878.

Huong, H.T.L. and Pathirana, A., 2013. Urbanization and climate change impacts on future urban flooding in Can Tho city, Vietnam. *Hydrology and Earth System Sciences*, *17*(1), p.379.

Krajewski, W. F., Villarini, G., & Smith, J. A. (2010). Radar-Rainfall Uncertainties: Where are We after Thirty Years of Effort? *Bulletin of the American Meteorological Society*, *91*(1), 87–94. https://doi.org/10.1175/2009BAMS2747.1

Manabe, S., & Wetherald, R. T. (1975). The Effects of Doubling the CO2 Concentration on the climate of a General Circulation Model. *Journal of the Atmospheric Sciences, 32*(1), 3-15. doi:10.1175/1520-0469(1975)0322.0.co;2

Modrick, T. M., & Georgakakos, K. P. (2015). The character and causes of flash flood occurrence changes in mountainous small basins of Southern California under projected climatic change. *Journal of Hydrology: Regional Studies, 3,* 312-336. doi:10.1016/j.ejrh.2015.02.003

Moscrip, A. L., & Montgomery, D. R. (1997). Urbanization, Flood Frequency, And Salmon Abundance In Puget Lowland Streams. *Journal of the American Water Resources Association, 33*(6), 1289-1297. doi:10.1111/j.1752-1688.1997.tb03553.x

National Research Council. (2005). *Flash flood forecasting Over Complex Terrain: With an Assessment of the Sulphur Mountain NEXRAD in Southern California*. Washington, D.C.: National Academies Press. doi:10.17226/11128

Oakley, N. S., Cannon, F., Munroe, R., Lancaster, J. T., Gomberg, D., & Ralph, F. M. (2018). Brief communication: Meteorological and climatological conditions associated with the 9 January 2018 post-fire debris flows in Montecito and Carpinteria, California, USA. *Natural Hazards and Earth System Sciences, 18*(11), 3037-3043. doi:10.5194/nhess-18-3037-2018

Oakley, N. S., Lancaster, J. T., Kaplan, M. L., & Ralph, F. M. (2017). Synoptic conditions associated with cool season post-fire debris flows in the Transverse Ranges of southern California. *Natural Hazards, 88*(1), 327-354. doi:10.1007/s11069-017-2867-6

Persad, G. G., Swain, D. L., Kouba, C., & Ortiz-Partida, J. P. (2020). Inter-model agreement on projected shifts in California hydroclimate characteristics critical to water management. *Climatic Change*. doi:10.1007/s10584-020-02882-4

Prein, A. F., Rasmussen, R. M., Ikeda, K., Liu, C., Clark, M. P., & Holland, G. J. (2016). The future intensification of hourly precipitation extremes. *Nature Climate Change, 7*(1), 48-52. doi:10.1038/nclimate3168

Ralph, F. m., Dettinger, M., White, A., Reynolds, D., Cayan, D., Schneider, T., Cifelli, R., Redmond, K., Anderson, M., Gherke, F., Jones, J., Mahoney, K., Johnson, L., Gutman, S., Chandrasekar, V., Lundquist, J., Molotch, N., Brekke, L., Pulwarty, R., … Wick, G. (2014). A Vision for Future Observations for Western U.S. Extreme Precipitation and Flooding. *Journal of Contemporary Water Research & Education*, *153*(1), 16–32. https://doi.org/10.1111/j.1936-704X.2014.03176.x

Ritchie, H., Samborska, V., & Roser, M. (2024, February 21). *Urbanization*. Our World in Data. https://ourworldindata.org/urbanization

San Diego County Flood Control Advisory Commission. (2003). *San Diego County Hydrology Manual* (Rep.). San Diego, CA: County of San Diego Department of Public Works Flood Control Section.

Smith, B. K., & Smith, J. A. (2015). The Flashiest Watersheds in the Contiguous United States. *Journal of Hydrometeorology*, *16*(6), 2365–2381. https://doi.org/10.1175/JHM-D-14-0217.1

Smith, J. A., Miller, A. J., Baeck, M. L., Nelson, P. A., Fisher, G. T., & Meierdiercks, K. L. (2005). Extraordinary flood response of a small urban watershed to short-duration convective rainfall. *Journal of Hydrometeorology, 6*(5), 599-617. doi:10.1175/jhm426.1

Sukup, S., Laber, J., Sweet, D., & Thompson, R. (2016). *Analysis of an Intense Narrow Cold Frontal Rainband and the Springs Fire Burn Area Debris Flows of 12 December 2014* (p. 32). National Weather Service, Forecast Office. https://www.weather.gov/media/wrh/online_publications/TAs/TA1601.pdf

Swain, D. L. (2021). A Shorter, Sharper Rainy Season Amplifies California Wildfire Risk. *Geophysical Research Letters, 48*(5). doi:10.1029/2021gl092843

Swain, D. L., Langenbrunner, B., Neelin, J. D., & Hall, A. (2018). Increasing precipitation volatility in twenty-first-century California. *Nature Climate Change, 8*(5), 427-433. doi:10.1038/s41558-018-0140-y

Swain, D. L., Wing, O. E., Bates, P. D., Done, J. M., Johnson, K. A., & Cameron, D. R. (2020). Increased Flood Exposure Due to Climate Change and Population Growth in the United States. *Earth's Future, 8*(11). doi:10.1029/2020ef001778

Tang, J. (2025). *jntp/Catchcore: Catchcore v1.0* (Version 1.0) [Computer software]. Zenodo. https://doi.org/10.5281/zenodo.15036761

Tang, J. (2025). *jntp/masters-scripts: Masters-scripts v1.0* (Version 1.0) [Computer software]. Zenodo. https://doi.org/10.5281/zenodo.14957524

Thackeray, C. W., DeAngelis, A. M., Hall, A., Swain, D. L., & Qu, X. (2018). On the Connection Between Global Hydrologic Sensitivity and Regional Wet Extremes. *Geophysical Research Letters, 45*(20). doi:10.1029/2018gl079698

Thompson, R. A. (2001). *Flash Flood Event of 6 February 1998: A Case Study* (Western Region Technical Assessment 01–08). National Weather Service, Western Region. https://www.weather.gov/media/wrh/online_publications/TAs/ta0108.pdf

Thornton, M.M., R. Shrestha, Y. Wei, P.E. Thornton, S. Kao, and B.E. Wilson. 2020. Daymet: Daily Surface Weather Data on a 1-km Grid for North America, Version 4. ORNL DAAC, Oak Ridge, Tennessee, USA. https://doi.org/10.3334/ORNLDAAC/1840

UNDRR. (2020). *The human cost of disasters: An overview of the last 20 years (2000-2019)*. https://www.undrr.org/publication/human-cost-disasters-overview-last-20-years-2000-2019

U.S. Census Bureau QuickFacts. (n.d.). *U.S. Census Bureau QuickFacts: California; South El Monte city, California; El Monte city, California; United States*. Retrieved January 1, 2022.

US Department of Commerce, N. (n.d.). *Product Descriptions*. NOAA's National Weather Service. Retrieved June 14, 2024, from https://www.weather.gov/box/product_descriptions

USGS. (n.d.). Floods: Recurrence intervals and 100-year floods. Retrieved March 26, 2021, from Floods: Recurrence intervals and 100-year floods

Viale, M., Houze, R. A., & Rasmussen, K. L. (2013). Upstream Orographic Enhancement of a Narrow Cold-Frontal Rainband Approaching the Andes. *Monthly Weather Review, 141*(5), 1708-1730. doi:10.1175/mwr-d-12-00138.1

Westra, S., Fowler, H. J., Evans, J. P., Alexander, L. V., Berg, P., Johnson, F., . . . Roberts, N. M. (2014). Future changes to the intensity and frequency of short-duration extreme rainfall. *Reviews of Geophysics*, *52*(3), 522-555. doi:10.1002/2014rg000464

Wilson, J. W., & Brandes, E. A. (1979). Radar Measurement of Rainfall—A Summary. *Bulletin of the American Meteorological Society*, *60*(9), 1048–1060. https://doi.org/10.1175/1520-0477(1979)060<1048:RMORS>2.0.CO;2

Wolfe, D. L., Conkle, C., & Moyer, J. (2006). *Hydrology Manual* (Rep.). Alhambra, CA: Los Angeles County Department of Public Works.

Yang, L., Smith, J. A., Baeck, M. L., & Zhang, Y. (2016). Flash flooding in small urban watersheds: Storm event hydrologic response. *Water Resources Research, 52*(6), 4571-4589. doi:10.1002/2015wr018326

Yang, L., Smith, J., Baeck, M. L., Smith, B., Tian, F., & Niyogi, D. (2016). Structure and evolution of flash flood producing storms in a small urban watershed. *Journal of Geophysical Research: Atmospheres, 121*(7), 3139-3152. doi:10.1002/2015jd024478

Tables

Table 1

Basin Characteristics of the Four Urban Watersheds

Basin Characteristic	Sepulveda	Whittier Narrows	Santa Ana River	San Diego River
Total Drainage Area	455.1 km^2	327.9 km^2	6363.9 km^2	1116.3 km^2
Urban Land Coverage	73.3%	70.2%	35.9%	26.2%
Impervious Coverage	30.3%	34%	13%	10.6%
Mean Elevation	1139 m	381 m	828 m	567 m
Relief	967 m	1812 m	3481 m	1947 m
Mean Basin Slope	14.2%	19.8%	20.7%	22.4%
Mean Annual Precipitation	455 mm	574 mm	500 mm	495 mm

Table 2

Streamflow Thresholds

	Sepulveda	Whittier Narrows	Santa Ana River	San Diego River
Streamflow (m^3 s^{-1})	209	202	107	41

Chosen streamflow flood thresholds for each urban watershed based on the median (2-year return interval) of the maximum annual streamflows. Streamflows, in addition to FFWs during the same time period, exceeding these thresholds during storm events are considered urban flood events.

Table 3

List of Items in NCFR Catalog (de Orla-Barile et al., 2022)

Item	File Type	Brief Description
Southern California NCFR Catalog (1995-2020)	csv	Each entry is a Southern California NCFR event. Includes information on the date, time of NCFR appearance on radar imagery, and other geographic and temporal characteristics.
ERA5 Synoptic Meteorology Plots	png	Contains two sets of plots for each NCFR event. One set displays the 850 hPa potential equivalent temperature (θ_e); the other set displays the 250 hPA integrated water vapor (IWV).
NCFR Propagation Stats	csv	Displays the hourly propagation statistics for 10 NCFR events. Statistics include distance, speed, azimuth as well as maximum reflectivity values.
NEXRAD Composites	png	Contains composites, or the average of the maximum reflectivity of each grid cell, of 91 out of 94 NCFR events.
Processed Reflectivity Data	nc	Consists of 78 NEXRAD level-II datasets, processed and gridded. Each file displays the radar loop of an NCFR propagating through Southern California.

Table 4

Various Threshold Values for Segmenting NCFRs on Radar Imagery

Threshold	Value
Minimum Reflectivity	45 dbZ*
Minimum Size of Convective Cells	100 pixels
Maximum Size of “Small Holes”	3 pixels
Maximum Cell Width	80 pixels
Maximum Distance for Centroids to be “Adjacent”	100 pixels
Minimum Slope along x-axis for Cells to not be “Adjacent”	1
Maximum Distance along y-axis for Cells to be Associated	25 pixels
Maximum Radius for Cells to be “Connected”	30 pixels
Minimum Major Axis (NCFR) Length	250 pixels
Maximum Area of “Small Cells”	1800 pixels

Table 4 shows the various maximum or minimum threshold values used to segment NCFRs on radar imagery. Pixel thresholds were obtained via trial-and-error and chosen based on the most successful results. Radar and watershed data were plotted on a pseudo-plate carrée projection, which allowed for the use of a geographic coordinate system where x coordinates represented the longitude and y coordinates represented the latitude.

*45 dbZ was the default threshold; however, occasionally 35 and 45 dbZ threshold were used when the default threshold failed to return an output.

Table 5

Selected RAWS Sites

RAWS Site	Watershed	WFO	Coordinates	Elevation	Time Period
Cheeseboro	Sepulveda Dam	LOX	34°11'05"N, 118°43'02"W	503 m	1995 to 2020
Santa Fe Dam	Whittier Narrows Dam	LOX	34°07'15"N, 117°56'45"W	152 m	1995 to 2020
Fremont Canyon	Santa Ana River	SGX	33°48'29"N, 117°42'40"W	543 m	1995 to 2020
Camp Elliot	San Diego River	SGX	32°51'33"N, 117°06'20"W	164 m	2004 to 2020

Table 6

Multiple Regression – Maximum Reflectivity (Z), Azimuth (a), Speed (v) vs. Peak Streamflow

Watershed	Regression Equation	P-values	R^2
Sepulveda Dam	$Q = -579.8 + 15.991*Z - 2.093*a - 11.154*v + \varepsilon$	const: 0.141 Z: 0.027 a: 0.055 v: 0.059	0.32408
Whittier Narrows Dam	$Q = -56.474 + 2.954*Z - 0.426*a - 3.722*v + \varepsilon$	const: 0.707 Z: 0.271 a: 0.308 v: 0.121	0.10921
Santa Ana River	$Q = -216.37 + 3.892*Z + 0.503*a + 1.41*v + \varepsilon$	const: 0.379 Z: 0.370 a: 0.457 v: 0.712	0.06947
San Diego River	$Q = -107.48 + 1.624*Z + 0.296*a + 1.052*v + \varepsilon$	const: 0.084 Z: 0.136 a: 0.084 v: 0.270	0.24022

Table 7

Multiple Regression – Maximum Reflectivity (Z), Azimuth (a), Speed (v) vs. Runoff Ratio

Watershed	Regression Equation	P-values	R^2
Sepulveda Dam	$r = 0.593 - 0.093*Z - 0.171*a - 25.421*v + \varepsilon$	const: 0.092 Z: 0.055 a: 0.104 v: 0.638	0.48048
Whittier Narrows Dam	$r = 0.008 - 0.000*Z + 0.003*a - 0.377*v + \varepsilon$	const: 0.215 Z: 0.114 a: 0.678 v: 0.493	0.26389
Santa Ana River	$r = 0.000 + 0.000*Z + 0.004*a - 0.059*v + \varepsilon$	const: 0.399 Z: 0.808 a: 0.372 v: 0.030	0.34018
San Diego River	$r = -0.009 + 0.001*Z + 0.009*a + 0.474*v + \varepsilon$	const: 0.355 Z: 0.281 a: 0.613 v: 0.373	0.23928

Figures

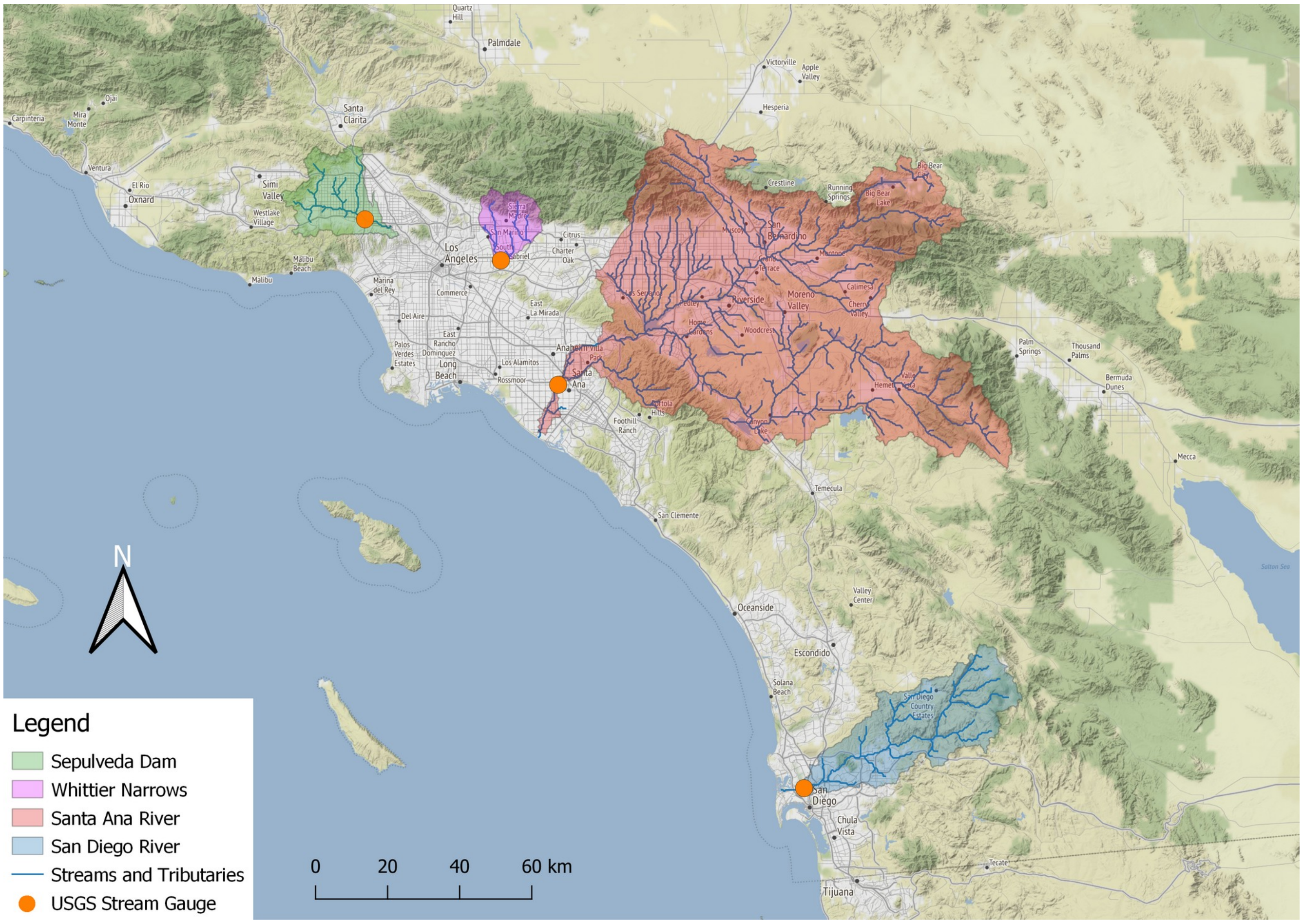

Fig. 1

Fig. 1 shows a map of southwestern California, including the Los Angeles metropolitan area (where the northern three watersheds are located) and the San Diego metropolitan area (where the southernmost watershed is located), along with the four chosen urban watersheds for study. Note that the white-gray shading represents urban land cover and the green shading represents elevation (the darker the green, the higher the elevation).

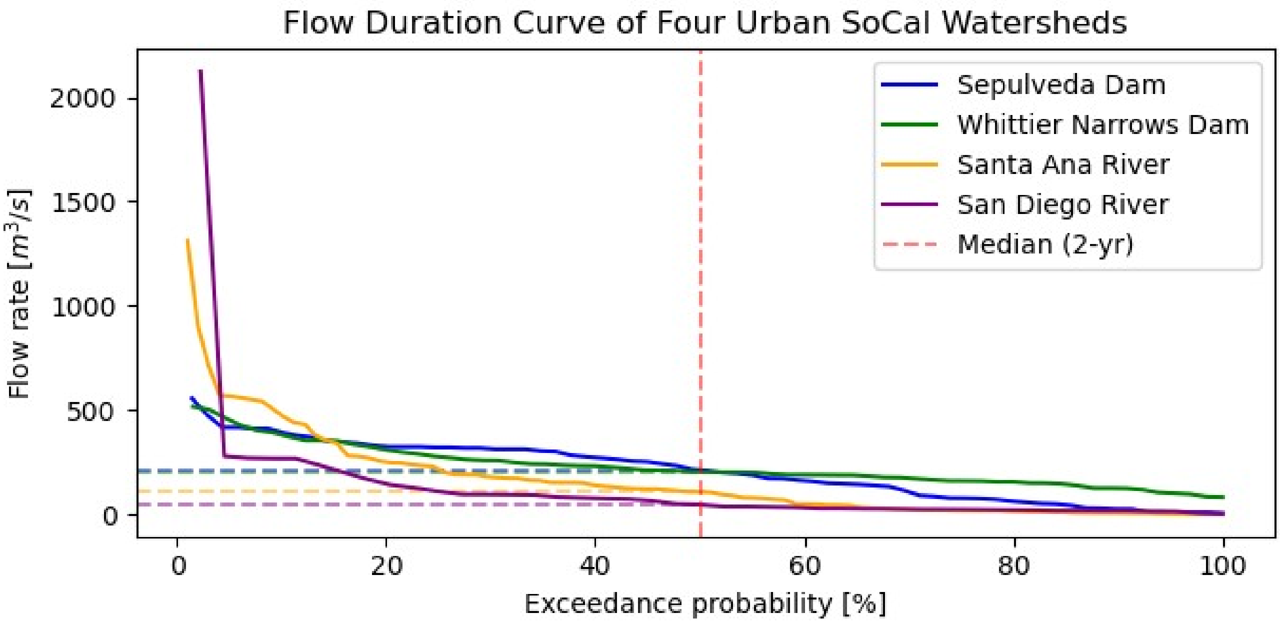

Fig. 2

Annual peak streamflow exceedance probability for all four watersheds. Median values (pink dashed line) were used as the threshold for flooding.

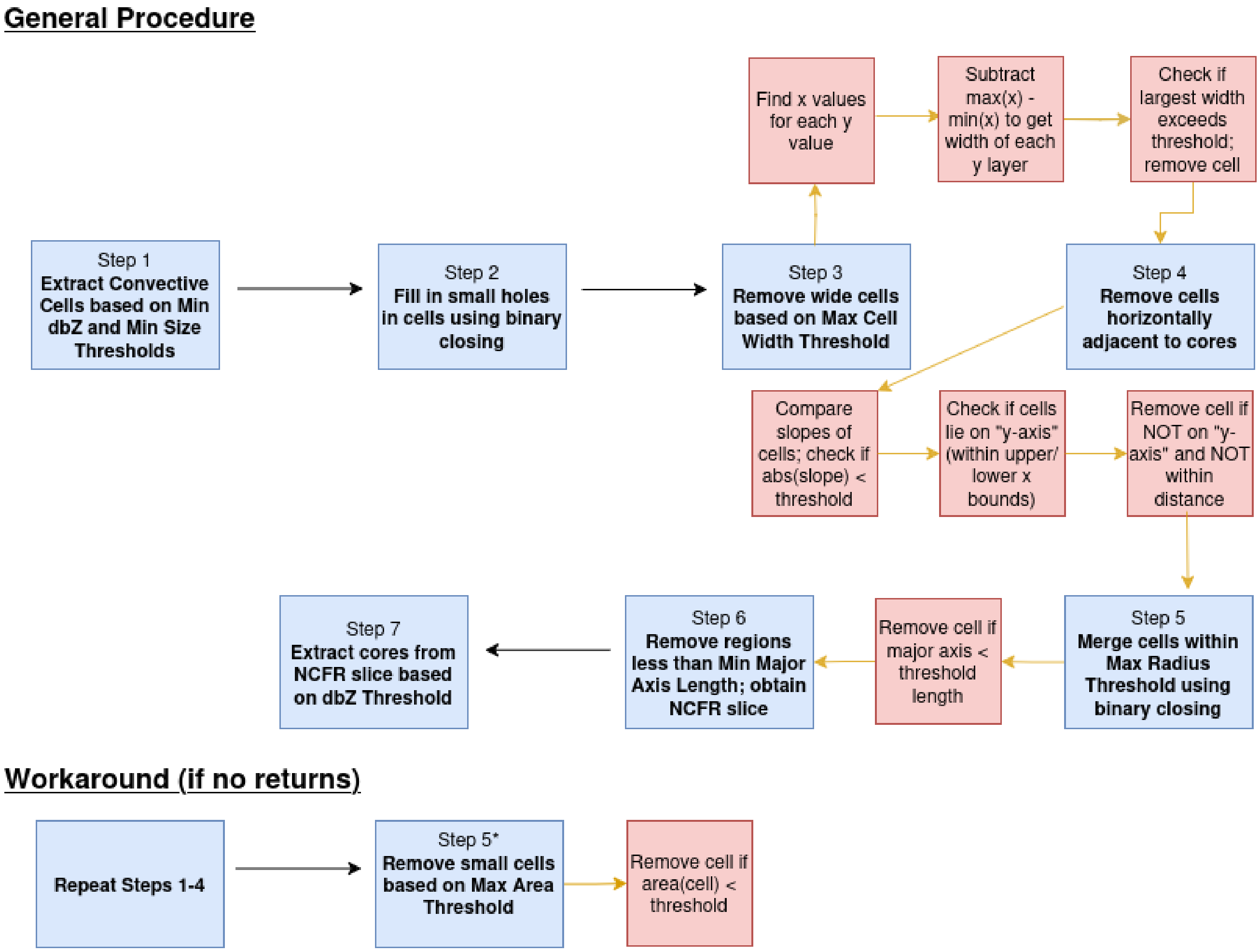

Fig. 3

Flow chart of the seven-step segmentation procedure to identify and delineate NCFR cores on radar imagery. A shorter, five-step "workaround" procedure is followed if the initial procedure fails to detect any NCFR cores. This workaround procedure removes labeled cells whose area is smaller than a set threshold, which usually results in extracted NCFR cores. An "NCFR slice" refers to the delineated NCFR in its entirety, including the gaps and cores. "Horizontally adjacent" refers to any cells in close proximity to an NCFR core so that it appears horizontal or nearly horizontal (close to the x-axis) to the NCFR core. Abs(slope) refers to the absolute value of the slope between adjacent cells, and area(cell) refers to the area of the cell.

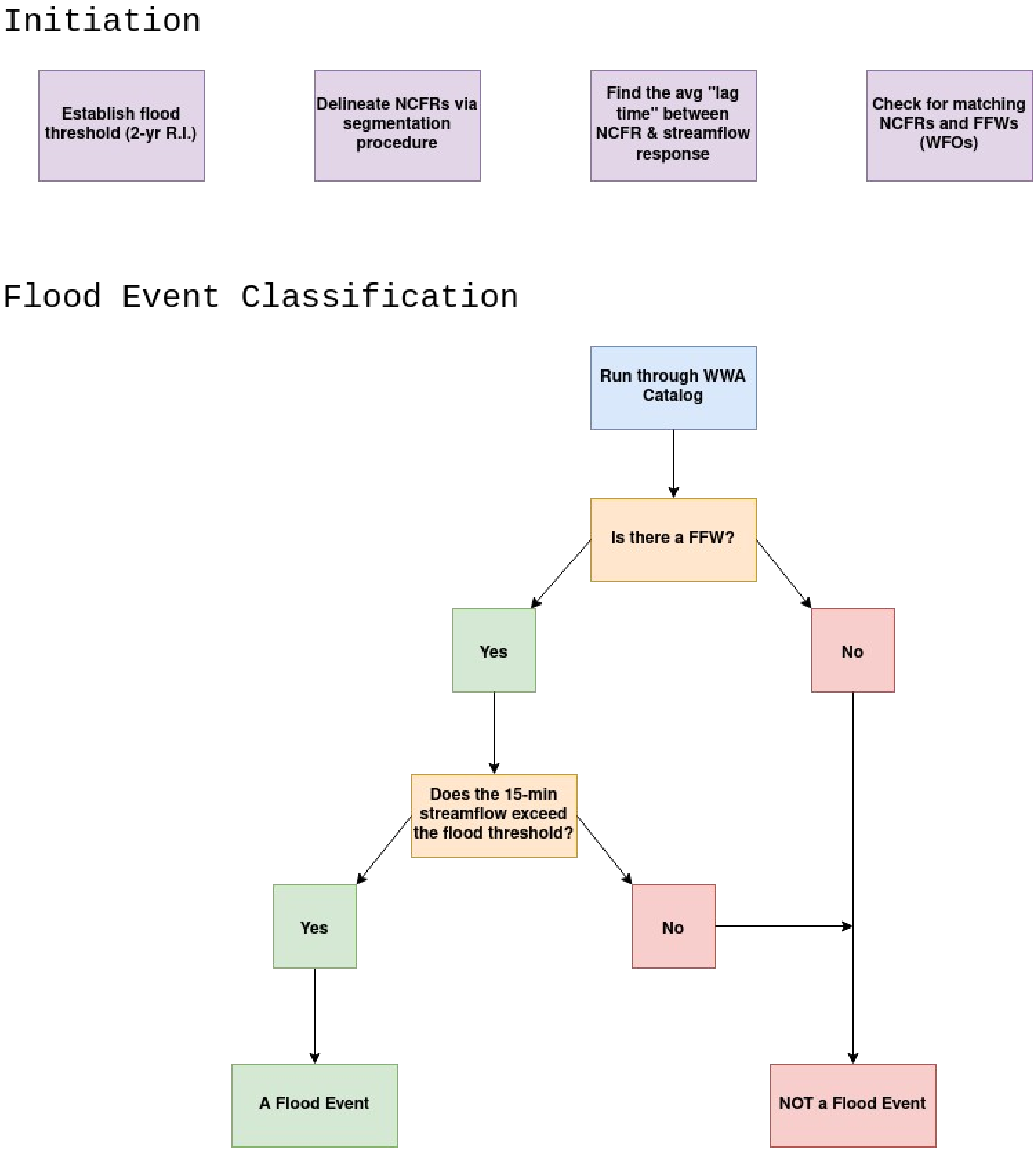

Fig. 4

Fig. 4 shows the procedure and logic behind classifying flood events. Initiation refers to the preliminary steps taken before flood event classification and NCFR flood event classification. If all conditions are met during the classification process, then a flood event is considered to have occurred.

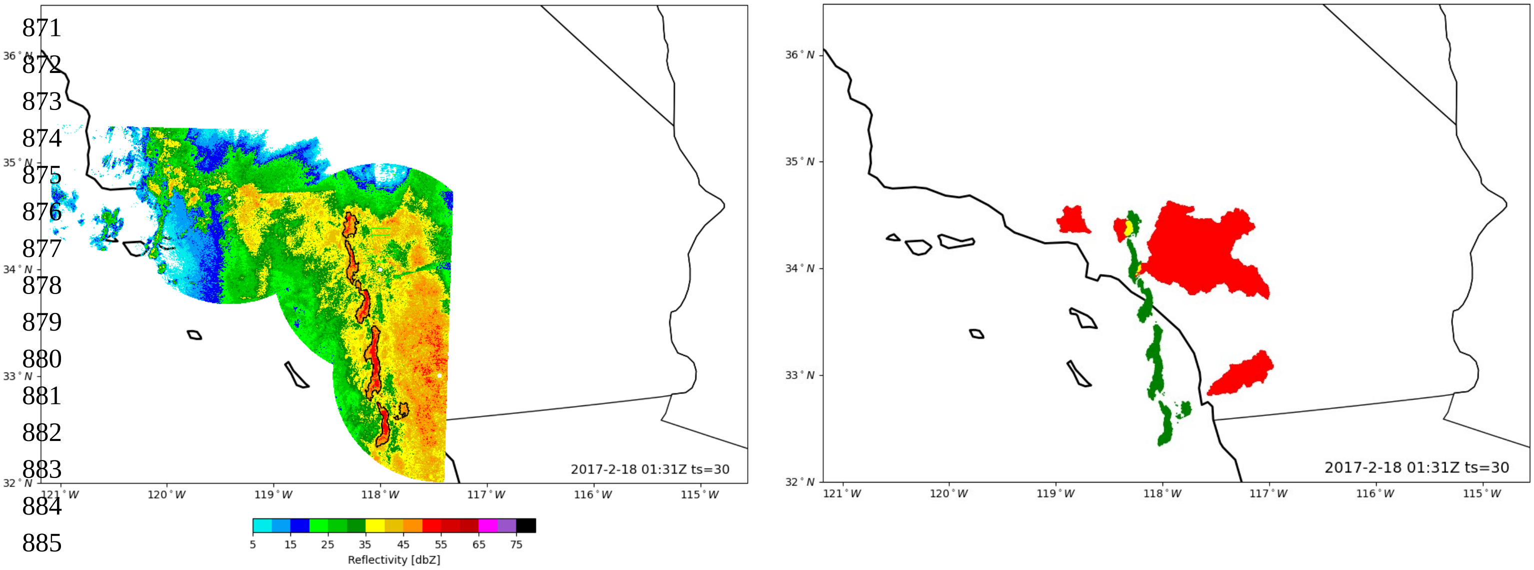

Figs 5a and 5b

Fig. 5a (left) shows the segmented NCFR cores over a single time frame during the 17-18 Feb 2017 atmospheric river event. Fig. 5b (right) shows the polygonized cores (green) and its intersections (yellow) with the watersheds (red) during the same time frame.

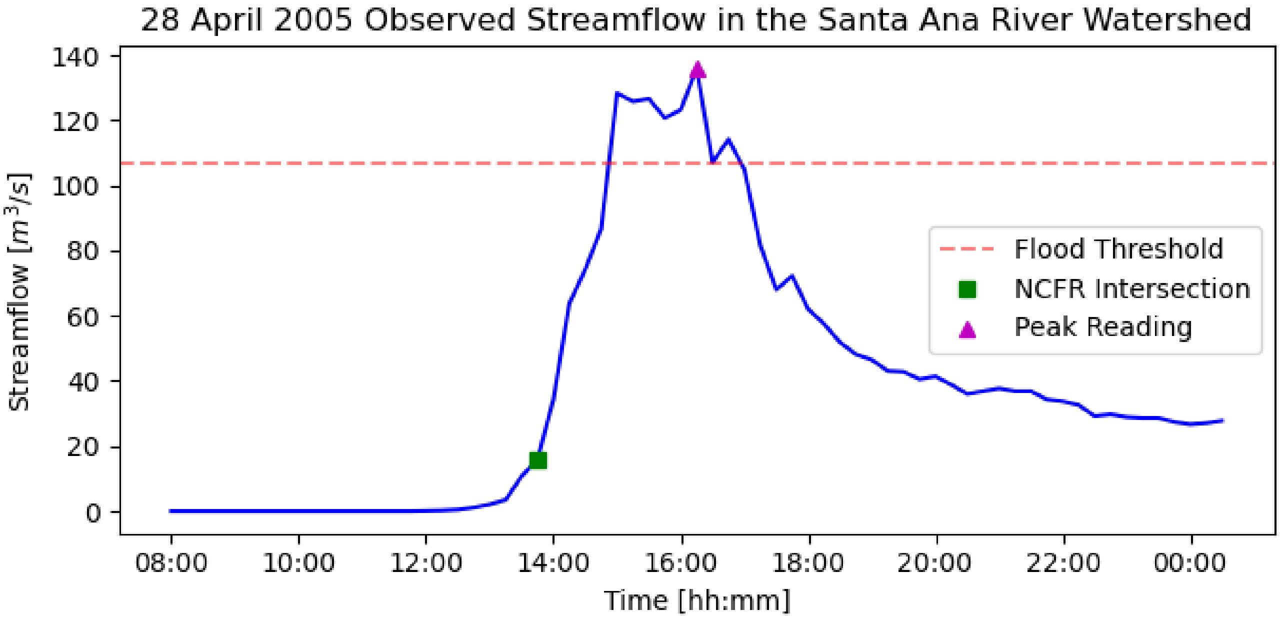

Fig. 6

Fig. 6 shows the observed streamflow in the Santa Ana River watershed during the 28 April 2005 storm event. Shortly after the NCFR passed near 14:00 UTC, the watershed saw dramatic rises in streamflow that exceeded the flood threshold. This event was one of the 11 flood events caused by an NCFR.

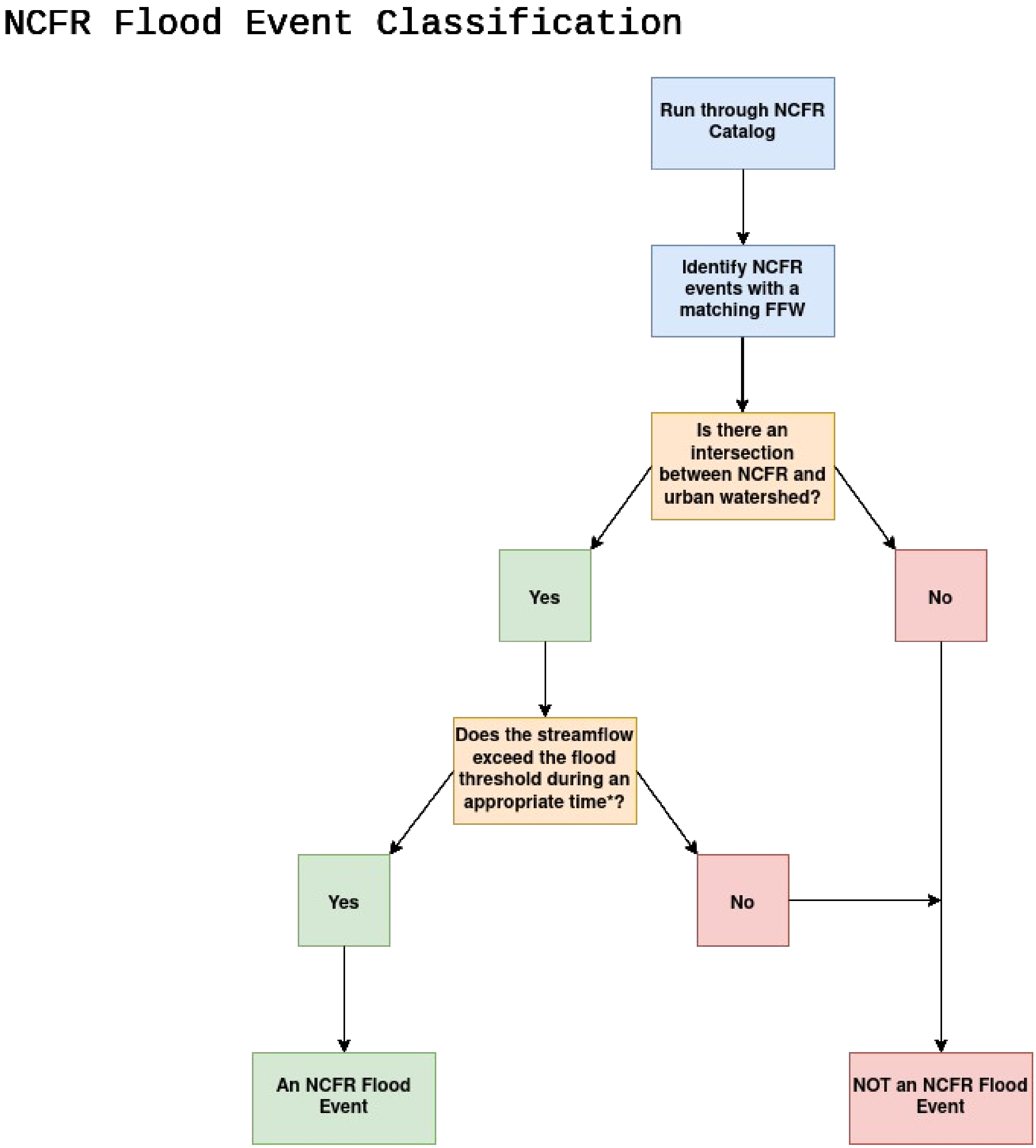

Fig. 7

Fig. 7 shows the procedure and logic behind NCFR flood classification. If all conditions are met, then the NCFR event is considered to be the cause of urban flooding in Southern California.

*Appropriate time refers to the time within a few hours of the NCFR passage (see Tables 9-12 for the average streamflow response time for each urban watershed). Based off the hydrograph of the observed streamflow, some NCFR events were not considered the cause of urban flooding despite exceeding the flood threshold if the streamflows were already high due to prior heavy rain.

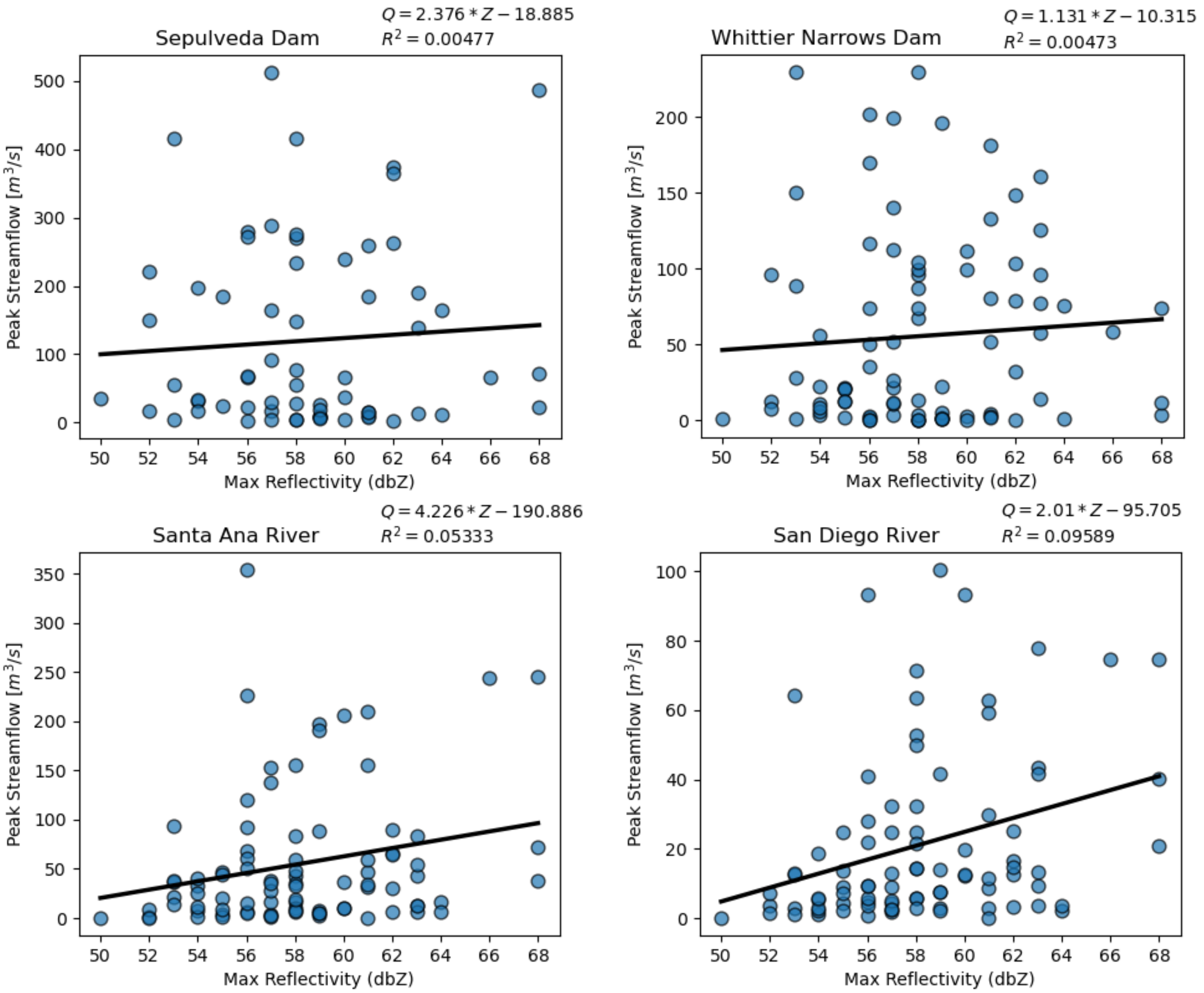

Figs. 8

Maximum reflectivity versus peak streamflow of the Sepulveda Dam (upper left, Fig. 8a), Whittier Narrows Dam (upper right, Fig. 8b), Santa Ana River (lower left, Fig. 8c), and the San Diego River (lower right, Fig. 8d) watersheds

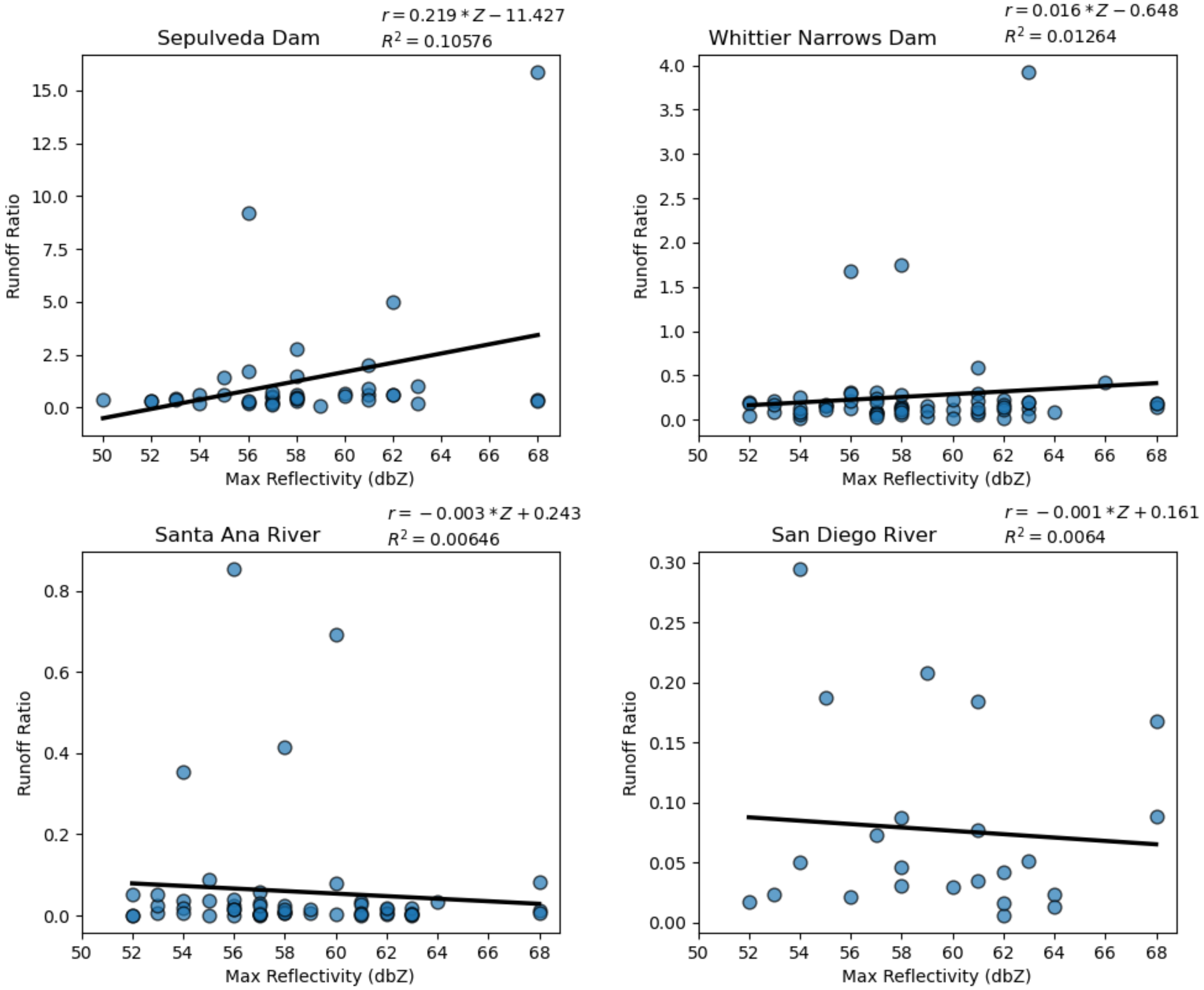

Fig. 9

Maximum reflectivity versus runoff ratio of the Sepulveda Dam (upper left, Fig. 9a), Whittier Narrows Dam (upper right, Fig. 9b), Santa Ana River (lower left, Fig. 9c), and the San Diego River (lower right, Fig. 9d) watersheds

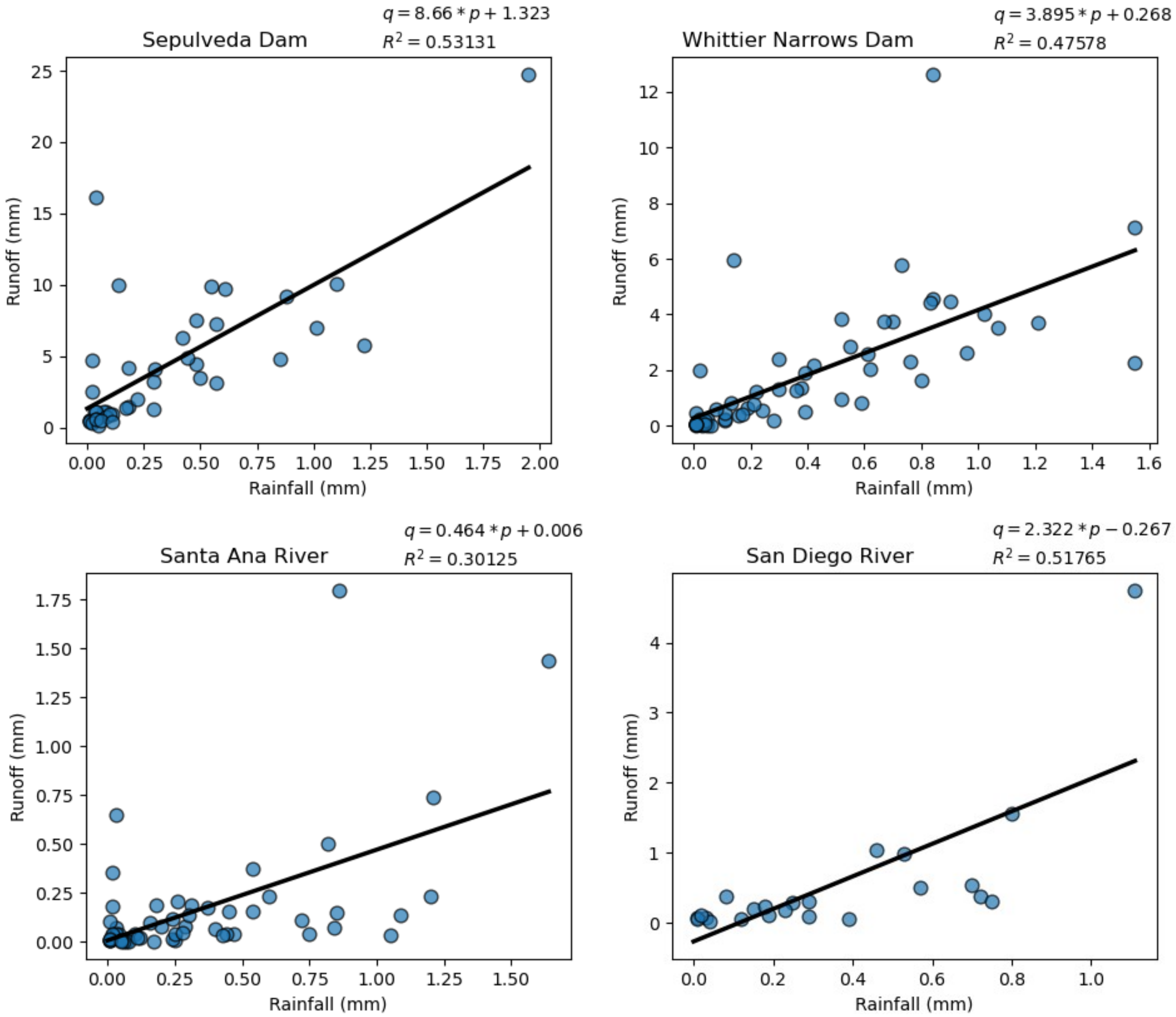

Figs. 10

Rainfall versus runoff of the Sepulveda Dam (upper left, Fig. 10a), Whittier Narrows Dam (upper right, Fig. 10b), Santa Ana River (lower left, Fig. 10c), and the San Diego River (lower right, Fig. 10d) watersheds

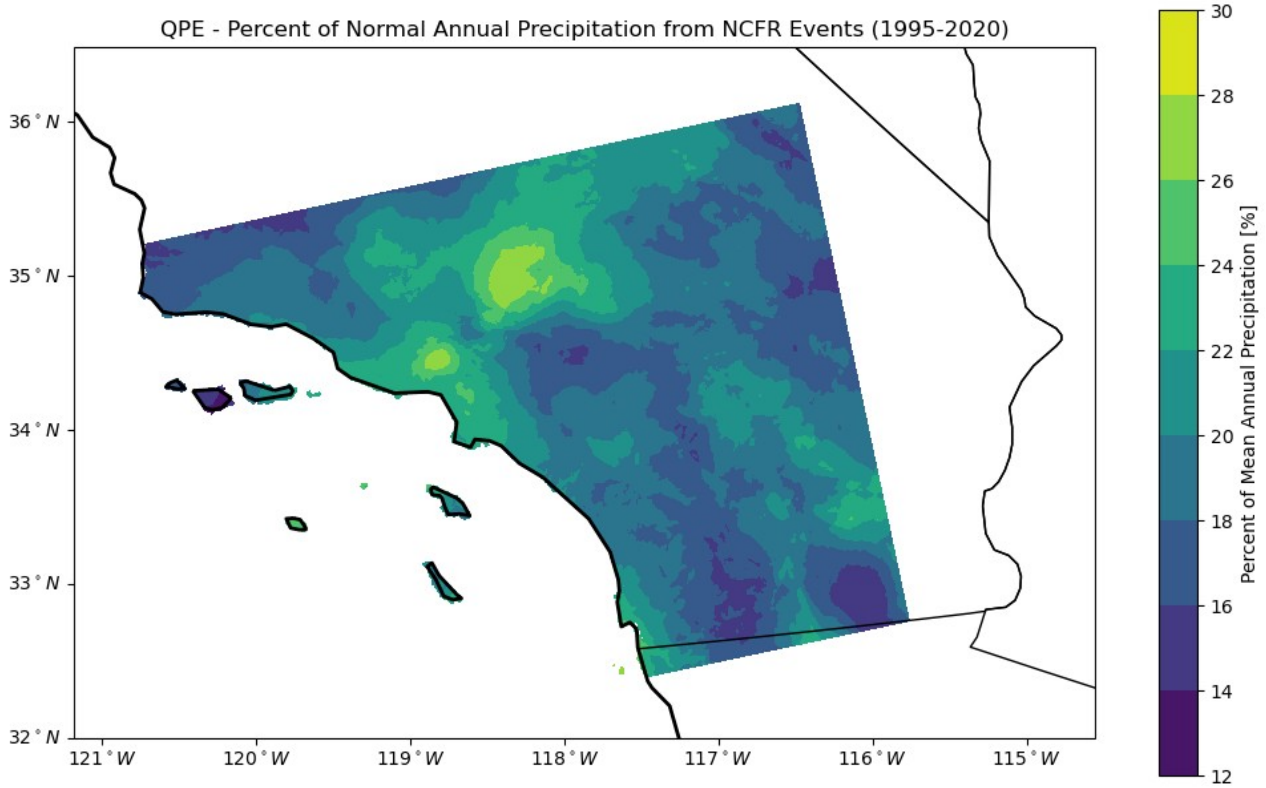

Fig. 11

Fig. 11 shows a QPE map of the percent of average annual precipitation attributed to NCFR events (total precipitation from NCFR events divided by the annual climatological normal) in Southwestern California from 1995-2020.

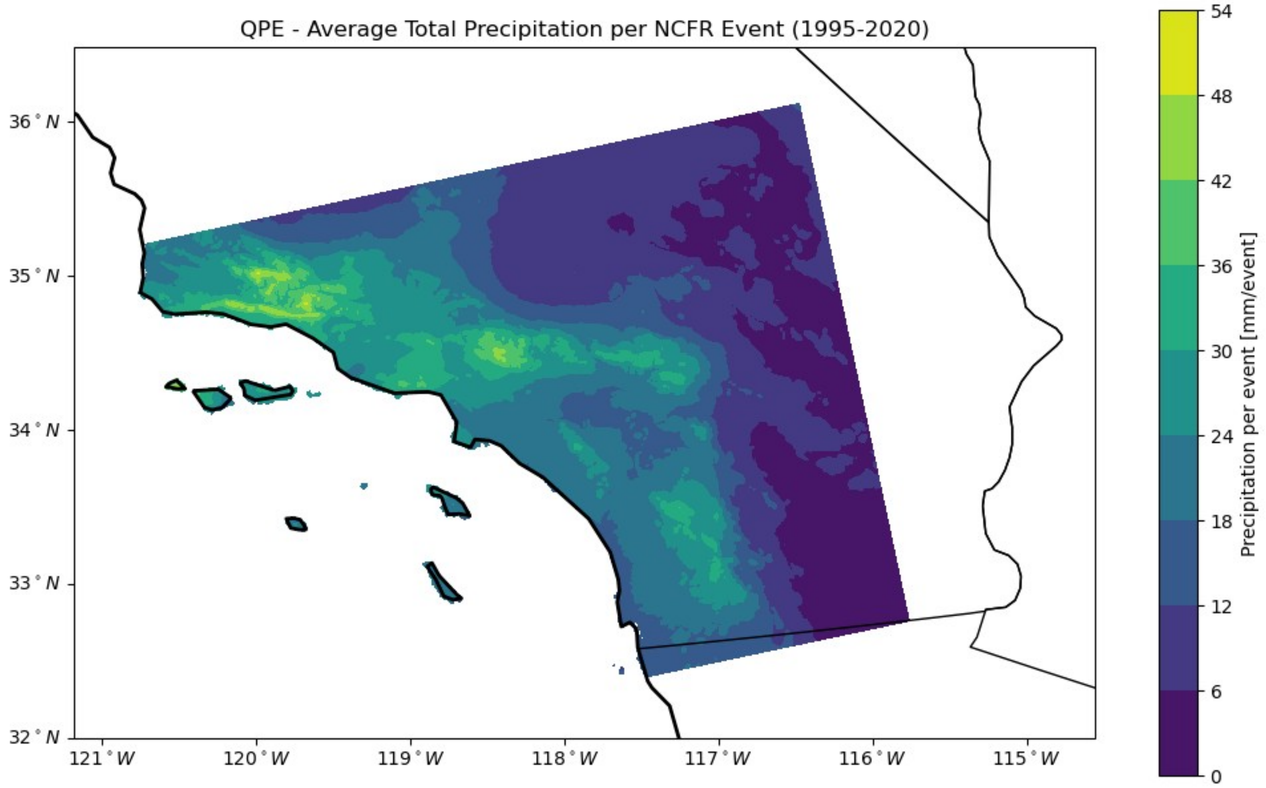

Fig. 12

Fig. 12 shows a QPE map of the average total precipitation from NCFR events (total precipitation from NCFR events divided by the number of NCFR events) in Southwestern California from 1995-2020.

Supplementary Information

Table 8

NCFRs, FFWs, and Watershed Intersections

Index	Date of NCFR Start	NCFR Start	NCFR End	FFW Start	FFW End	WFO	Crosses Watershed?	Watersheds Crossed
1	1995 Jan 25	10:00	12:00	11:00	17:00	LOX	FALSE	
4	1997 Jan 12	22:00	01:00	09:00	11:00	SGX	TRUE	SD
6	1998 Feb 3	09:00	15:00	12:48	16:45	LOX	TRUE	SP
7	1998 Feb 3	13:00	18:00	19:50	23:00	LOX	TRUE	SP
8	1998 Feb 3	14:00	21:00	19:50	23:00	LOX	TRUE	SD
9	1998 Feb 6	14:00	18:00	20:00	21:00	LOX	TRUE	SD
11	1998 Mar 25	18:00	23:00	21:29	22:30	SGX	TRUE	SD
18	2000 Feb 21	03:00	06:00	04:50	08:00	LOX	TRUE	SA
19	2000 Feb 21	15:00	18:00	21:45	23:45	SGX	FALSE	
20	2000 Feb 23	21:00	01:00	21:20	23:00	LOX	TRUE	SD
22	2001 Jan 11	02:00	08:00	08:00	11:00	LOX	TRUE	WN, SD
26	2002 Dec 20	00:00	05:00	07:12	09:00	LOX	FALSE	
29	2003 Dec 26	01:00	03:00	01:52	06:00	SGX	FALSE	
30	2004 Feb 3	05:00	08:00	06:26	09:30	SGX	TRUE	SA, SD
31	2004 Oct 20	13:00	19:00	16:01	18:00	SGX	TRUE	SD
32	2004 Oct 27	06:00	14:00	06:01	09:00	SGX	TRUE	SA, SD
33	2004 Feb 28	05:00	08:00	06:08	07:30	LOX	FALSE	
34	2004 Feb 28	08:00	12:00	12:39	14:30	LOX	FALSE	
35	2004 Feb 28	13:00	18:00	13:58	17:00	LOX	TRUE	SP, SA, SD
36	2004 Feb 29	06:00	09:00	13:46	16:00	SGX	TRUE	SA
37	2004 Feb 29	10:00	13:00	13:46	16:00	SGX	TRUE	SD
38	2005 Feb 21	10:00	16:00	15:43	18:00	SGX	FALSE	
39	2005 Feb 21	15:00	19:00	15:43	18:00	SGX	TRUE	SD
40	2005 Apr 28	11:00	15:00	12:52	15:00	SGX	TRUE	SA
42	2006 Jan 2	17:00	22:00	18:37	00:30	SGX	TRUE	SP, WN, SA
43	2006 Mar 3	16:00	18:00	16:04	18:00	LOX	TRUE	SA
45	2006 Apr 5	03:00	06:00	09:18	11:00	SGX	TRUE	SA, SD
48	2006 Dec 10	01:00	08:00	04:44	05:45	LOX	TRUE	WN
51	2008 Jan 23	23:00	05:00	03:22	04:15	LOX	FALSE	
57	2010 Jan 18	22:00	01:00	00:00	01:00	SGX	TRUE	SA, SD
59	2010 Jan 20	23:00	04:00	23:42	02:30	LOX	FALSE	
60	2010 Apr 11	23:00	13:00	07:36	10:01	LOX	TRUE	WN
61	2010 Nov 21	09:00	18:00	09:23	10:45	LOX	TRUE	SP, WN
63	2011 Mar 20	09:00	17:00	22:00	00:45	LOX	FALSE	

Index	Date of NCFR Start	NCFR Start	NCFR End	FFW Start	FFW End	WFO	Crosses Watershed?	Watersheds Crossed
64	2011 Mar 20	23:00	05:00	00:47	02:45	LOX	TRUE	SP
72	2014 Feb 28	16:00	20:00	23:18	00:15	SGX	TRUE	SA
73	2014 Feb 28	21:00	01:00	23:18	00:15	SGX	TRUE	SD
74	2014 Dec 12	06:00	14:00	07:04	08:30	LOX	TRUE	SP, WN, SA
75	2016 Jan 31	18:00	00:00	21:59	01:00	SGX	FALSE	
76	2016 Mar 7	08:00	17:00	12:44	14:15	LOX	TRUE	SP, WN
77	2016 Mar 11	18:00	01:00	19:42	21:30	LOX	TRUE	SP, WN
78	2017 Jan 20	19:00	00:00	22:38	01:30	SGX	FALSE	
79	2017 Feb 17	22:00	04:00	22:23	01:15	LOX	TRUE	SP, WN, SA, SD
80	2018 Jan 9	07:00	15:00	10:56	15:00	LOX	FALSE	
81	2019 Jan 5	20:00	09:00	05:40	07:27	LOX	FALSE	
86	2019 Feb 2	13:00	01:00	22:35	01:30	SGX	FALSE	
87	2019 Feb 4	12:00	19:00	17:27	19:48	LOX	FALSE	
89	2019 Nov 28	15:00	20:00	17:22	20:15	SGX	TRUE	SA, SD

Table 8 shows the NCFR events that share common times with at least one WFO-issued FFWs and checks whether NCFR cores have crossed the urban watersheds of interest. Only NCFRs that have a FFW issued in between their start or end time, or up to 2 hours, 50 minutes (this was based on the average length of FFWs as calculated from the WWA catalog) were listed and selected for further assessment. Start and end times of NCFRs and FFWs are based on UTC time. Intersection of NCFR cores and watersheds were also checked for NCFR events with matching FFW times. Note that SP, WN, SA, and SD stand for Sepulveda Dam, Whittier Narrows Dam, Santa Ana River, and San Diego River—respectively. Events meeting all criteria were selected for streamflow assessment (See Tables 9-12).

Table 9

NCFR Streamflow Assessment – Sepulveda Dam

Index	Time of Intersection	Initial Time	Initial Streamflow	Peak Time	Peak Streamflow	NCFR Flood?
6	1998-02-03 12:53:00	No data	No data	No data	No data	False
7	1998-02-03 14:43:00	No data	No data	No data	No data	False
35	2004-12-28 14:25:00	2004-12-28 14:30:00	343	2004-12-28 16:20:00	416	False
42	2006-01-02 18:21:00	2006-01-02 18:15:00	289	2006-01-02 18:45:00	329	False
61	2010-11-21 13:11:00	2010-11-21 13:15:00	2	2010-11-21 14:45:00	140	False
64	2011-03-21 00:36:00	2011-03-21 00:30:00	470	2011-03-21 02:30:00	555	False
74	2014-12-12 11:17:00	2014-12-12 11:15:00	17	2014-12-12 13:15:00	244	True
76	2016-03-07 14:00:00	2016-03-07 14:00:00	2	2016-03-07 16:00:00	165	False
77	2016-03-11 21:52:00	2016-03-11 21:45:00	2	2016-03-11 23:45:00	148	False

79	2017-02-18 00:21:00	2017-02-18 00:15:00	399	2017-02-18 00:22:00	459	False
	Average Response Time:	01:29:37				

Table 10

NCFR Streamflow Assessment – Whittier Narrows Dam

Index	Time of Intersection	Initial Time	Initial Streamflow	Peak Time	Peak Streamflow	NCFR Flood?
22	2001-01-11 09:10:00	2001-01-11 09:15:00	120	2001-01-11 10:00:00	202	True
42	2006-01-02 19:01:00	2006-01-02 19:00:00	123	2006-01-02 19:45:00	243	True
48	2006-12-10 03:35:00	2006-12-10 03:30:00	0	2006-12-10 05:45:00	1	False
60	2010-04-12 08:11:00	2010-04-12 08:15:00	159	2010-04-12 08:30:00	182	False
61	2010-11-21 14:01:00	2010-11-21 14:00:00	3	2010-11-21 15:15:00	113	False
74	2014-12-12 12:02:00	2014-12-12 12:00:00	1	2014-12-12 13:00:00	82	False
76	2016-03-07 14:45:00	2016-03-07 14:45:00	0	2016-03-07 16:00:00	75	False
77	2016-03-11 22:37:00	2016-03-11 22:30:00	0	2016-03-11 23:45:00	107	False
79	2017-02-18 01:01:00	2017-02-18 01:00:00	149	2017-02-18 02:00:00	217	False
	Average Response Time:	01:04:59				

Table 11

NCFR Streamflow Assessment – Santa Ana River

Index	Time of Intersection	Initial Time	Initial Streamflow	Peak Time	Peak Streamflow	NCFR Flood?
18	2000-02-21 04:41:00	2000-02-21 04:45:00	37	2000-02-21 06:15:00	78	False
30	2004-02-03 05:50:00	2004-02-03 05:45:00	3	2004-02-03 08:30:00	108	True
32	2004-10-27 07:46:00	2004-10-27 07:45:00	92	2004-10-27 09:45:00	142	True
35	2004-12-28 16:15:00	2004-12-28 16:15:00	2	2004-12-28 19:30:00	43	False
36	2004-12-29 09:25:00	2004-12-29 09:30:00	19	2004-12-29 12:15:00	87	False
40	2005-04-28 12:50:00	2005-04-28 12:45:00	16	2005-04-28 15:15:00	136	True
42	2006-01-02 19:51:00	2006-01-02 19:45:00	2	2006-01-02 23:15:00	43	False
43	2006-03-03 17:02:00	2006-03-03 17:00:00	2	2006-03-03 21:15:00	59	False
45	2006-04-05 06:45:00	2006-04-05 06:45:00	37	2006-04-05 09:45:00	38	False
57	2010-01-18 22:56:00	2010-01-18 23:00:00	93	2010-01-19 00:15:00	168	True
72	2014-02-28 18:02:00	2014-02-28 18:00:00	24	2014-02-28 19:45:00	71	False
74	2014-12-12 12:32:00	2014-12-12 12:30:00	3	2014-12-12 14:30:00	64	False
79	2017-02-18 01:56:00	2017-02-18 02:00:00	56	2017-02-18 04:00:00	129	True
89	2019-11-28 15:47:00	2019-11-28 15:45:00	0	2019-11-28 18:00:00	15	False
	Average Response Time:	02:28:55				

Table 12

NCFR Streamflow Assessment – San Diego River

Index	Time of Intersection	Initial Time	Initial Streamflow	Peak Time	Peak Streamflow	NCFR Flood?
4	1997-01-12 23:08:00	1997-01-12 23:15:00	2	1997-01-13 00:00:00	7	False
8	1998-02-03 17:38:00	1998-02-03 17:15:00	3	1998-02-03 19:15:00	9	False
11	1998-03-25 21:49:00	1998-03-25 21:45:00	1	1998-03-26 03:15:00	25	False
20	2000-02-24 00:55:00	2000-02-24 01:00:00	6	2000-02-24 06:30:00	28	False
30	2004-02-03 07:25:00	2004-02-03 07:30:00	0	2004-02-03 17:30:00	6	False
31	2004-10-20 17:42:00	2004-10-20 17:45:00	12	2004-10-21 03:00:00	41	False
32	2004-10-27 11:10:00	2004-10-27 11:15:00	3	2004-10-27 17:30:00	71	True
35	2004-12-28 17:40:00	2004-12-28 17:45:00	5	2004-12-28 00:15:00	15	False
37	2004-12-29 10:45:00	2004-12-29 10:45:00	35	2004-12-29 14:30:00	78	True
39	2005-02-21 18:10:00	2005-02-21 18:15:00	26	2005-02-22 01:15:00	93	True
45	2006-04-05 05:00:00	2006-04-05 05:00:00	4	2006-04-05 12:15:00	11	False
57	2010-01-19 00:26:00	2010-01-19 00:30:00	1	2010-01-19 06:30:00	41	True
73	2014-03-01 00:32:00	No data	No data	No data	No data	False
79	2017-02-18 03:01:00	2017-02-18 03:00:00	2	2017-02-18 09:15:00	25	False
89	2019-11-28 19:12:00	2019-11-28 19:15:00	2	2019-11-28 01:30:00	40	True
	Average Response Time:	05:48:00				

Table 13

Hydrometeorological Parameters of NCFRs

Index	Date	Time (UTC)	Max dbZ	Peak Q SP ($m^3\ s^{-1}$)	Peak Q WN ($m^3\ s^{-1}$)	Peak Q SA ($m^3\ s^{-1}$)	Peak Q SD ($m^3\ s^{-1}$)	Runoff Ratio SP	Runoff Ratio WN	Runoff Ratio SA	Runoff Ratio SD
3	1996-10-30	06:00-23:00	63		2720	447	471		0.13	0	
4	1997-01-12	22:00-01:00	63		4430	1500	1530		0.2	0	
5	1997-11-26	16:00-20:00	53		1000	779	96		0.09	0.01	
6	1998-02-03	09:00-15:00	59		6920	6960	1470		0.16	0.01	
7	1998-02-03	13:00-18:00	63		3390	2950	1470		0.2	0.02	
8	1998-02-03	14:00-21:00	58		3390	2950	1870		0.14	0.02	
9	1998-02-06	14:00-18:00	62		3650	2320	443		0.22	0.01	
10	1998-02-20	00:00-06:00	55		723	1630	878		0.15	0.09	
11	1998-03-25	18:00-23:00	58		464	2100	876			0.41	
12	1998-05-12	17:00-01:00	61		4700	7410	298		0.59	0.03	
13	1998-11-28	10:00-12:00	55		751	114	152		0.17		
14	1998-11-28	12:00-15:00	57		751	114	152		0.08		
15	1999-01-31	11:00-18:00	54		115	263	41		0.02		
16	1999-03-15	13:00-18:00	54		376	36	71				
17	1999-03-25	13:00-18:00	56		1240	229	171		0.13	0	
19	2000-02-21	15:00-18:00	53		3130	3300	2270				

Index	Date	Time (UTC)	Max dbZ	Peak Q SP (m^3 s^{-1})	Peak Q WN (m^3 s^{-1})	Peak Q SA (m^3 s^{-1})	Peak Q SD (m^3 s^{-1})	Runoff Ratio SP	Runoff Ratio WN	Runoff Ratio SA	Runoff Ratio SD
20	2000-02-23	21:00-01:00	56		46	2400	984			0.02	
21	2000-03-05	17:00-20:00	55		46	720	479				
22	2001-01-11	02:00-08:00	56		7140	12500	771			0.04	
23	2001-03-06	07:00-10:00	55		723	1550	321			0.02	
24	2001-03-06	09:00-13:00	57		115	1330	321				
25	2001-11-12	22:00-03:00	56		75	192	23			0.06	
26	2002-12-20	00:00-05:00	56	9870	4120	4230	129				
27	2002-12-28	23:00-03:00	61	552	1830	11	100	0.27	0.21	0.04	
28	2003-04-14	21:00-00:00	57	603	376	4880	875	2	0.06	0	
30	2004-02-03	05:00-08:00	56	114	11	550	198	0.56	0.08	0.03	
31	2004-10-20	13:00-19:00	56	781	0	3240	1440				
32	2004-10-27	06:00-14:00	58	2720	0	5490	2520				
33	2004-12-28	05:00-08:00	53	14700	8120	477	445	1.74			
34	2004-12-28	08:00-12:00	58	14700	8120	1510	513	0.63			
35	2004-12-28	13:00-18:00	58	9570	3510	600	513	0.41	0.21		
36	2004-12-29	06:00-09:00	63	4890	5670	1900	2750	2.8	0.05		
37	2004-12-29	10:00-13:00	58	1970	2390	1240	2250	1.47	1.75		
38	2005-02-21	10:00-16:00	56	272.44	170.2	226.28	93.46	1.04	3.93		
39	2005-02-21	15:00-19:00	60	67.12	111.86	206.17	93.46	0.32	0.16		
40	2005-04-28	11:00-15:00	59	9.12	22.06	88.92	13.91	9.19	1.68	0.85	
41	2005-11-09	11:00-15:00	50	35.97	0.82	0	0.11		0.12	0.69	
42	2006-01-02	17:00-22:00	54	32	6	32.57	5.49				
43	2006-03-03	16:00-18:00	53	4.87	0.62	36.25	1.1	0.36			
44	2006-03-21	07:00-12:00	58	3.88	0.28	10.45	5.75	0.59	0.06	0.04	0.29
45	2006-04-05	03:00-06:00	53	54.94	150.1	37.95	12.94				
46	2006-05-21	21:00-05:00	56	66.27	50.13	60.89	9.26				0.09
47	2006-05-22	07:00-11:00	56	67.97	73.63	50.13	9.26	0.36	0.17	0.05	0.02
48	2006-12-10	01:00-08:00	55	23.87	12.26	1.25	2.32	0.22	0.31	0.02	0.02
49	2007-02-22	16:00-22:00	52	149.53	96	1.53	3.48	0.31	0.29	0.02	
50	2007-04-20	17:00-00:00	58	27.67	3.26	6.23	5.64	1.42	0.15	0	0.19
53	2009-02-13	17:00-02:00	54	33.7	22.06	25.88	2.92	0.35	0.19	0	0.02
54	2009-02-16	16:00-19:00	60	36.53	2.21	36.82	12.32		0.29	0.01	0.05
55	2009-12-07	22:00-01:00	58	4.53	0.31	7.82	49.84				
56	2009-12-13	10:00-12:00	60	4.98	0.37	10.22	19.71				
57	2010-01-18	22:00-01:00	61	9.12	3.85	156.04	62.87		0.12	0.35	0.05
58	2010-01-19	17:00-23:00	66	65.7	58.62	244.4	74.76	0.66	0.02	0.08	
59	2010-01-20	23:00-04:00	68	23.11	3.65	245.82	74.76				
60	2010-04-11	23:00-13:00	61	184.36	181.81	46.73	11.64				
61	2010-11-21	09:00-18:00	63	14.19	14.08	5.69	9.29	0.62	0.29	0.03	0.08
62	2011-02-26	08:00-13:00	61	8.07	2.21	59.47	29.74		0.42		
63	2011-03-20	09:00-17:00	57	512.59	112.71	0.88	1.7	0.36	0.18	0.08	0.17
64	2011-03-20	23:00-05:00	68	487.1	74.2	71.65	20.67	15.87	0.14	0.01	0.09
65	2011-11-06	17:00-21:00	57	3.79	140.75	2.95	2.38		0.24	0	
66	2011-11-20	12:00-04:00	60	239.3	99.4	10.17	12.69	0.53	0.22	0	0.03

Index	Date	Time (UTC)	Max dbZ	Peak Q SP ($m^3 s^{-1}$)	Peak Q WN ($m^3 s^{-1}$)	Peak Q SA ($m^3 s^{-1}$)	Peak Q SD ($m^3 s^{-1}$)	Runoff Ratio SP	Runoff Ratio WN	Runoff Ratio SA	Runoff Ratio SD
67	2012-03-17	18:00-21:00	59	8.07	1.9	7.56	7.56	0.11	0.03	0.01	
68	2012-03-25	16:00-01:00	58	147.83	86.66	18.63	2.72	0.43	0.13	0.01	0.03
69	2012-04-13	13:00-23:00	62	373.82	148.68	30.59	3.34	4.97	0.17	0	0.01
70	2012-12-13	11:00-18:00	62	2.46	0.2	6.46	16.48		0.02		0.04
71	2013-03-08	09:00-13:00	64	11.5	0.85	16.51	2.01				0.02
72	2014-02-28	16:00-20:00	61	258.84	80.43	31.44	0	0.37	0.09	0	
73	2014-02-28	21:00-01:00	57	91.19	26.39	16.51	13.03	0.19	0.2	0	0.07
74	2014-12-12	06:00-14:00	62	263.09	78.45	89.21	14.73	0.59	0.11	0.01	0.02
75	2016-01-31	18:00-00:00	59	8.5	0.82	2.89	2.97				
76	2016-03-07	08:00-17:00	64	164.54	75.33	5.81	3.74		0.09	0.03	0.01
77	2016-03-11	18:00-01:00	59	26.65	4.7	5.35	2.01				0.21
78	2017-01-20	19:00-00:00	59	18.32	1.16	191.44	100.54		0.11		
79	2017-02-17	22:00-04:00	62	365.33	32.28	64.85	25.26	0.63	0.15	0.02	
80	2018-01-09	07:00-15:00	58	274.99	103.93	32.85	21.38	0.5	0.12	0.01	
81	2019-01-05	20:00-09:00	57	164.26	52.11	27.92	5.18	0.27	0.07	0.01	
82	2019-01-12	03:00-12:00	63	189.46	57.21	12.8	3.57	0.22	0.05	0	
83	2019-01-14	17:00-19:00	55	185.5	12.63	8.3	7.25	0.59	0.11		
84	2019-01-14	16:00-20:00	52	220.61	12.63	8.3	7.25	0.31	0.19	0.05	
85	2019-01-31	11:00-22:00	58	233.92	73.92	47.58	32.28	0.44	0.08	0.01	
86	2019-02-02	13:00-01:00	57	288.86	199.66	152.93	32.28	0.71	0.06	0.02	
87	2019-02-04	12:00-19:00	54	197.96	55.79	40.78	18.49		0.09	0.02	
88	2019-11-27	13:00-16:00	52	17.62	7.11	0.34	1.53		0.05	0	
89	2019-11-28	15:00-20:00	68	70.8	11.7	38.52	40.21	0.34	0.18	0.01	
90	2019-12-23	12:00-15:00	59	5.35	0.99	4.9	7.65				
91	2019-12-26	09:00-16:00	61	14.36	1.53	33.7	59.19		0.13		
92	2020-03-16	22:00-06:00	54	16.88	7.93	11.5	5.92	0.18	0.26	0.01	
93	2020-03-23	03:00-09:00	57	28.89	11.38	34.83	2.35	0.14	0.03	0	

Table 10 shows the hydrological and meteorological parameters of 88 NCFR events. Max dbZ refers to the maximum reflectivity reported over any watershed of interest. The next eight columns show the peak streamflow and runoff ratio of each of the four watersheds.

Table 14

Propagation Statistics of 30 NCFR Events

Index	Date	Time (UTC)	Start TS	Start Position	End TS	End Position	Distance (km)	Azimuth (°)	Speed (m/s)
0	1996-10-30	18:41-19:41	22	(-117.660, 32.635)	34	(-117.399, 32.795)	30.21	54.1	8.39
1	1997-01-12	22:48-23:08	21	(-117.223, 32.860)	27	(-117.051, 32.833)	16.34	100.49	9.08
2	1997-11-26	16:24-16:49	6	(-118.354, 34.097)	9	(-118.237, 34.106)	10.84	84.69	12.04
3	1998-02-03	14:11-15:11		(-118.677, 33.884)		(-118.354, 34.07)	36.28	55.26	10.08
4	1998-02-06	16:32-17:32		(-119.296, 33.9)		(-118.963, 34.29)	53.06	35.29	14.74
5	1998-11-28	10:46-11:46	21	(-120.103, 34.023)	33	(-119.906, 34.140)	22.33	54.5	6.2
6	1999-03-15	14:25-15:25	16	(-117.969, 32.714)	28	(-117.696, 33.031)	43.45	36.01	12.07

Index	Date	Time (UTC)	Start TS	Start Position	End TS	End Position	Distance (km)	Azimuth (°)	Speed (m/s)
7	2001-11-12	23:21-23:46	4	(-119.354, 34.237)	9	(-119.177, 34.230)	16.34	92.57	10.89
8	2002-12-29	01:26-02:26	40	(-119.729, 34.281)	52	(-119.276, 34.376)	43.05	75.81	11.96
9	2003-04-14	22:10-23:10	26	(-117.357, 32.856)	38	(-117.0214, 32.878)	31.46	85.37	8.74
10	2004-10-20	17:17-17:47	27	(-117.257, 32.874)	33	(-117.003, 32.900)	24.02	82.78	13.34
11	2005-11-09	12:30-13:30	30	(-119.907, 34.091)	42	(-119.830, 34.286)	22.79	18.03	6.33
12	2006-01-02	19:46-20:46	23	(-117.839, 32.775)	35	(-117.358, 33.105)	58	50.73	16.11
13	2006-03-21	08:40-09:40	44	(-117.444, 32.756)	56	(-117.067, 32.793)	35.56	83.87	9.88
14	2008-12-26	00:00-00:15	24	(-117.910, 33.940)	27	(-117.808, 33.814)	16.85	145.86	18.72
15	2009-12-07	22:57-23:27	23	(-117.585, 33.264)	29	(-117.192, 33.437)	41.29	62.22	22.94
16	2009-12-13	10:41-11:31	20	(-117.918, 33.938)	30	(-117.677, 33.734)	31.79	135.41	10.6
17	2010-01-19	21:30-22:30		(-117.959, 33.266)		(-117.362, 33.52)	62.28	62.94	17.3
18	2010-01-21	00:30-01:30		(-117.866, 32.849)		(-117.202, 33.085)	67.37	66.96	18.71
19	2010-11-21	12:14-13:14		(-119.528, 33.675)		(-118.982, 33.592)	51.49	100.15	14.3
20	2011-02-26	10:44-11:44		(-117.611, 33.163)		(-117.199, 33.253)	39.69	75.32	11.02
21	2011-03-21	02:51-03:51		(-117.546, 32.696)		(-117.215, 33.112)	55.56	33.78	15.43
22	2012-03-17	19:30-20:30		(-117.569, 32.954)		(-117.089, 33.244)	55.16	54.2	15.32
23	2012-03-25	22:47-23:47		(-117.629, 32.734)		(-117.274, 33.085)	51.17	40.37	14.21
24	2012-12-13	12:21-12:51	28	(-117.244, 32.765)	34	(-117.214, 32.752)	3.15	118.29	1.75
25	2013-03-08	10:45-11:20	21	(-117.394, 32.784)	28	(-117.172, 33.129)	43.59	28.33	20.76
26	2014-12-12	11:19-12:19		(-118.311, 33.707)		(-117.922, 33.839)	38.89	67.78	10.8
27	2017-01-20	17:02-17:32	0	(-120.049, 34.562)	6	(-119.789, 34.515)	24.41	102.3	13.56
28	2017-02-18	01:31-02:31	30	(-117.701, 33.015)	42	(-117.336, 32.959)	34.73	100.23	9.65
29	2018-01-09	09:00-10:00	0	(-120.819, 34.621)	12	(-120.573, 34.731)	25.7	61.58	7.14

Table 14 shows the propagation statistics of 30 NCFR events, 10 of which were obtained from the NCFR Catalog (de Orla Barile et al., 2020) and 20 of which were obtained from the segmentation procedure. For the 20 NCFR events obtained from the segmentation procedure, a core was tracked (usually over 12 timesteps or 1 hour interval) with the starting timestep marked as “Start TS” and the ending timestep marked as “End TS.” The distance, azimuth (direction), and speed were calculated based on the difference in centroid position between the starting and ending timesteps.